Author Comment to manuscript egusphere-2023-2140, (https://doi.org/10.5194/egusphere-2023-2140, in review, 2023): "Updating the radiation infrastructure in MESSy (based on MESSy version 2.55)"

by M. Nützel et al.

February 9, 2024

We thank the referees for taking the time to review our paper. We are grateful for their comments which helped to improve the manuscript. In the following we address each review comment (*black italics*) by stating our reply (blue). In addition we append a manuscript version which highlights the changes between the preprint version of the manuscript and the revised version.

Reply to comments from editor

In addition to the comments by the reviewers, the editor has commented on our discussion version and requested these comments to be considered in a revised version. We thank the editor for these comments which we will address below.

Minor comments on egusphere-2023-2140

1. Abstract: The statement "they also aim towards the use of MESSy with the ICOsahedral Non- hydrostatic (ICON) model" is unclear. I think it means that the use of this development will be feasible in the MESSy infrastructure,

using ICON as the base model, but it should be more clearly written.

We rephrased the sentence which now reads: "The developments presented here also aim towards the use of the MESSy infrastructure with the ICOsahedral Non-hydrostatic (ICON) model as a base model." We hope that this removes any ambiguities.

2. Line 27: Correct spelling of "asessed"

Done.

3. Line 55: No need for "radiative" in front of "RFs"

Done.

4. Line 190: I would recommend changing "supposed to follow". Often, the word "supposed" can have a negative context, i.e., something was planned, but it didn't actually happen! How about "this functionality is due to be implemented with a revision of the AEROPT submodel"?

Done.

5. Line 255: Change "Still missing" to "Any remaining missing"

Done.

6. Line 278/298: Change "via namelist" to "via a namelist"

Done.

7. Line 296: Change "where shifted" to "were shifted"

Done.

8. Line 469: Please provide full name for JJA on first use (Same applies for DJF on line 476)

Done.

9. Line 523: Please correct the bracketing

We could not find any bracketing that needs correction in line 523. The formula for calculating relative anomalies is correct and we assume that the bracket "(panels b and d)" is also ok.

10. Line 660: I suggest that you replace "guideline" with "guiding principle".

Done.

Reply to comments from CEE

(https://doi.org/10.5194/egusphere-2023-2140-CEC1)

The executive editor has commented on our discussion version. We will address this comment below.

Dear authors,

Please, in any potential reviewed version of your manuscript provide in the "Code Availability" section a link to the MESSY private repository in Zenodo, including its DOI.
Best regards,
Juan A. Añel
Geosci. Model Dev. Executive Editor

We thank the executive editor for this comment. The respective reference is now included in the "Code Availability" Section. Please note that these updates are not highlighted in the appended diff-version.

Reply to comments from Referee #1 (https://doi.org/10.5194/egusphere-2023-2140-RC1)

Below we will address all comments of referee #1 and we will state corresponding changes in the manuscript. Again, we would like to thank referee #1 for taking the time to review our manuscript and for the thoughtful comments.

This paper is, in part, a technical report of the updated infrastructure concerning the treatment of radiation in the Modular Earth Submodel System (MESSy), and in part, an evaluation of the performance of the newly implemented PSrad (Pincus and Stevens) radiation scheme vs. the ECHAM5 radiation scheme. It is clearly written with sufficient technical detail to be useful for developers of the MESSy infrastructure as well as serving as a useful example for developers of other model radiation schemes.

The evaluation of the radiation schemes serves as a good test of the implementation and a useful evaluation of two schemes side-by-side in an identical model. The only problematic area is the comparison of the schemes against reference data presented in Pincus et al (2020), based on RFMIP (Radiative Forcing Model Intercomparison Project).

I would recommend this paper for publication once the following, generally minor comments have been addressed:

We thank the reviewer for this general rating of our manuscript. We revised our document according to the suggestions given by the reviewer and here we reply to each of the comments. In particular we tried to adjust the comparison to reference data. If we did not follow the suggestions at some particular instance we hope that our respective replies make our choice understandable.

Principal comment:

1) Section 4, lines 630-640: The arguments presented here may be valid but it feels like the overall argument in this section is biased towards achieving a better comparison for the PSrad scheme. I think a more robust comparison could be done avoiding the need for the caveats in this section.

In the previous paragraph, lines 613-628, you use your present-day (PD) background runs to compare with the Pincus et al results for the forcing from pre-industrial to present-day GHG amounts. You scale the quantities to account for the different PD background conditions which sounds reasonable. For the CO2-folding experiments, however, you revert to the pre-industrial (PI) background runs. Your following arguments detail why this is a bad thing to do. Given that you have a range of CO2-folding experiments for the PD-background runs: CO2(pi), CO2(pd), 2xCO2(pd), 4xCO2(pd), you should be able to interpolate values for 2xCO2(pi) and 4xCO2(pi) to directly compare with Pincus et al. It would then be good to have all the Pincus et al results listed in table 7 to provide a clear comparison for the reader.

We thank the reviewer for this comment and in particular for bringing the option of using our pd background simulation for comparison to our attention. We think that scaling the pi-pd results is reasonable, which can be seen as a comparison of radiative efficiencies. With respect to the CO_2-folding experiments, we referred to the pi simulation in which we did CO_2(pi)-folding experiments because this minimizes the differences between the sampling points with respect to which RF is calculated. We thought that this might be the first point to go to when comparing our study to the results by Pincus et al. (2020). Hence we warrant, that this of course comes at the drawback of having a different background. Doing the analysis the other way round - as suggested by the reviewer - leads to a comparable (pd) background at the expense of having the CO_2-folding experiments at sampling points which are quite different from the ones used in Pincus et al. (2020). As we were driven by comparing at similar sampling points, we completely disregarded the option raised by the reviewer. We now added a figure to our paper and discuss this second option. Nevertheless, we will also keep the discussion of the first option as we think it is good to put this approach into perspective and to outline the possible caveats.

Minor comments:

1) Section 1, line 89: "resulted in 0.23 Wm-2": please define what this number represents, i.e. define radiative forcing as the difference in which fluxes? Top-of-atmosphere / tropopause / surface. Directionality?

We corrected the respective sentence which now reads: "For instance, a doubling of the present-day reference value for methane of 1.8 μmol mol^{-1} resulted in a top-of-atmosphere stratospheric adjusted RF of 0.23 W m^{-2} (Winterstein et al., 2019; Stecher et al., 2021), while studies of Myhre et al. (1998) and Etminan et al. (2016) suggest 0.53 W m^{-2} and 0.62 W m^{-2}, respectively, for doubling of the reference value of 1.7 μmol mol^{-1}."

2) Section 2.4 CLOUDOPT: Can you provide some details on how the cloud fractions are handled. Do you have separate ice and liquid cloud fractions or are they mixed in a single cloud fraction? How is the vertical overlap of cloud fraction handled? (Maybe a reference for this is sufficient.)

In CLOUDOPT mass extinction coefficients for ice and liquid clouds are used to calculate the radiative properties (see lines 203-210 in the discussion paper). The cloud fraction, however, is not split into liquid and ice clouds (see the nml in the supplement of Dietmüller et al., 2016). With respect to the cloud overlap we added the following paragraph at the end of the CLOUDOPT section: "In CLOUDOPT and in the radiation schemes the (default) cloud overlap is assumed to be maximum-random overlap (Roeckner et al., 2003; Dietmüller et al., 2016; Giorgetta et al., 2018). In the case of PSrad the overlap assumption is treated based on the Monte Carlo Independent Column Approximation (McICA) technique (see Giorgetta et al., 2018, for details and further references)."

3) Section 2.5 ALBEDO, line 225: Please define what you mean by "blue-sky", "black-sky" and "white-sky" albedos. In other models, only the direct (your "black-sky" I think) and diffuse (your "white-sky") albedos are needed as the radiation scheme will solve for the direct and diffuse fluxes separately. Presumably the radiation schemes here don't do this and require a combined "blue-sky" albedo as well?

You are right, we use the terms white-sky and black-sky albedo which are relevant for the direct beam and isotropic diffuse radiation (Liu et al., 2009). The definitions are given in the papers referenced in L225. We have adapted this paragraph which now reads: "In particular, ALBEDO calculates a blue-sky albedo (α_{blue}) from the black-sky (α_{black}) and white-sky albedo (α_{white}) and the fraction of direct and diffuse radiation fluxes with respect

to the total downwelling shortwave fluxes at the surface ($f^{dir}_{sw,surf}$, $f^{dif}_{sw,surf}$) as $\alpha_{blue} = f^{dir}_{sw,surf}\,\alpha_{black} + f^{dif}_{sw,surf}\,\alpha_{white}$ (see e.g. Liu et al., 2009; Li et al., 2018; Cordero et al., 2021, and references therein for details on the different albedos and how to typically derive the blue-sky albedo). Here, the black-sky albedo relates to the albedo associated with the collimated beam, whereas the white-sky albedo corresponds to the albedo associated with isotropic diffuse radiation (Liu et al., 2009)."
Both radiation schemes separate between direct and diffuse flux as noted by Roeckner et al. (2003); Giorgetta et al. (2013). In the latter reference actually RRTMG is described, however PSrad was built based on RRTMG (Pincus and Stevens, 2013). In fact as explained in the text (and as you note in your comment below), the direct and diffuse fluxes are used to calculate the blue-sky albedo (see e.g. line 274 in the discussion paper). With some additional changes it would also be possible for us to pass the direct and diffuse albedos to the radiation schemes. This was, however, not considered in our current simulations but is a potential point of further investigation.

4) Section 2.5 ALBEDO: There is no mention of the spectral dependence of albedo. How is this handled by these schemes?

We do not apply any spectral dependent albedo neither in E5rad nor in PSrad. However, e.g. for PSrad we know that both direct and diffuse albedo can be separated into near-infrared and a UV-visible part. As stated before this might be an additional point for further investigation.

5) Section 2.5 Solar zenith angle dependent albedo, line 277: it would be good to explain at this point that you mean the fraction of diffuse and direct flux will be needed from a previous timestep call of the radiation scheme. What happens at model start-up when there is no previous call?

We added the respective information and also included the information that in the first model time step the partitioning of 0.9 (direct, black-sky) and 0.1 (diffuse, white-sky) albedo is used to calculate the blue-sky albedo. "To be able to use this new feature, either the radiation scheme has to provide (the fraction of) the direct and diffuse SW radiation fluxes from the previous model time step (for the first model time step the partitioning is automatically set to 0.9 and 0.1, respectively) or ..."

6) Section 2.6 (1): This appears to be an arbitrary functionality to add that could only degrade the physical accuracy of the results. Using the middle of the interval would appear to be the best of the options available. However, none of these options appear to consider what happens when the sun rises or sets during the radiation timestep. I believe the best approach (particularly for solar zenith angle) is to calculate the orbital parameters as a mean over the period of the timestep for which the sun is above the horizon. Was this considered?

We agree that this functionality seems odd without additional explanation: We included the new offset because we think it is the most reasonable. We kept the old implementation for backward compatibility. Further we added the option to select the offset freely for offline radiation calculations.

We adjusted the respective part: "Now, the offset type can be selected via a new namelist switch. Apart from the previous choice $\Delta t_{orb,opt0}$, which we kept to ensure backward compatibility, the orbital parameters now can be chosen to be calculated for the middle of the interval of time steps associated with the current radiation call ($t_{r,i-1}$, $t_{r,i-1} + \Delta t_m$,..., $t_{r,i} - \Delta t_m$, leading to $\Delta t_{orb,opt1} = \frac{1}{2}((t_{r,i} - \Delta t_m) - t_{r,i-1})$, Fig. 2b), or the offset can be set to an arbitrary constant ($\Delta t_{orb,con} \leq \Delta t_r$). The latter option was introduced for offline radiation calculations."

Regarding the problem of the rising or setting sun: For the radiation calculation the SZA is corrected such that its cosine cannot fall below a certain threshold (see equation 11.23 of Roeckner et al., 2003). Hence, the radiation is calculated globally with at least a certain minimum solar irradiation and later on corrected with the actual SZA (see equation 11.4 of Roeckner et al., 2003). We have incorporated this information in the respective section: "The results from this radiation call (with the adjusted orbital parameters) are later on corrected with the solar irradiation associated with the orbital parameters of the actual model time step for the calculation of the actual SW fluxes and heating rates (see Roeckner et al., 2003). We note that the adjusted SZA contains a modification which ensures that fluxes are non-zero globally to avoid problems in the grid boxes in which the sun rises or sets during the time steps associated with the radiation time step (see Roeckner et al., 2003, ; also their Eq. 11.23). "

7) Section 2.6 (2), lines 293-296: Not much point mentioning this adjustment unless you are going to explain how it was adjusted.

We removed the respective paragraph.

8) Section 3.1, line 340: It would be useful to give an approximate horizontal resolution in km for T42.

We rephrased the sentence: "The simulations were conducted with T42 spectral truncation (corresponding to about $2.8° \times 2.8°$, i.e. roughly $300\,\text{km} \times 300\,\text{km}$ at the equator) and 90 vertical levels extending up to roughly 80 km (see the T42L90MA setup e.g. mentioned by Jöckel et al., 2016)." We also added information on the time step length and the frequency of radiation calls, which we missed to give in the discussion version of the paper.

9) Section 3.1, line 357: "purely dynamic": I'm not sure what this means (in our usage, this would mean all the physics parametrisations are turned off, which is not the case here).

We thank the reviewer for pointing out this sloppy use of "dynamic". We have rephrased all such statements referring to the setups at hand as being of "GCM-type".

10) Section 3.2, paragraph at lines 433-444: I notice you specifically target clear-sky SW with albedo adjustments, but there is nothing to specifically target clear-sky LW. Is surface emissivity fixed for these schemes? Is there anything else that could be used to target this?

We thank the reviewer for pointing out this possibility. In principle it seems that the radiation schemes could deal with spectrally dependent and regionally varying surface emissivities. However, this is not a feature that is available. We would need to implement additional infrastructure to provide such an emissivity field to the radiation schemes and we would need to acquire the respective data beforehand. Hence, in our simulation we used our standard globally fixed surface emissivity of 0.996 as described by Roeckner et al. (2003). Apart from the surface emissivity we do not see any justifiable "tuning" parameter for clear-sky LW fluxes.

11) Section 4, line 550: Please explain how the stratospheric adjustment is done.

The stratospheric adjustment is calculated as described by Stuber et al. (2001) as stated in line 55 of the discussion paper. We have added this information also to the sentence in Section 4: "Table 5 lists the respective perturbations that are calculated in the multiple calls of the radiation scheme. In total, 22 additional (diagnostic) calls for calculating instantaneous RF (calls 02 to 23) and 11 additional calls for calculating stratospheric adjusted RF (calls 24 through 34, where stratospheric adjustment is calculated as described by Stuber et al., 2001), were conducted."

12) Section 4, line 619-620: "we assumed the 2014 values used by Pincus et al are similar to Meinshausn": I believe the values used by Pincus et al. are essentially those publicly available for RFMIP, so this assumption could be properly checked.

Pincus et al. (2020) mention that they use 2014 values from "NOAA greenhouse gas inventories". From this information we could not find the reference and the corresponding values and hence we assumed that they are close to the 2014 values presented by Meinshausen et al. (2017).

13) Section 4, line 628: the N2O RF presented by Pincus should be stated for comparison (even better, all the values from Pincus should be added to table 7).

We have added the respective value in the text and for the CO_2-folding experiments we added a new figure.

Typos etc.:

1) line 11: "of sixth generation of the the" → "of the sixth generation of the"

Done.

2) line 55: "radiative RFs" → "RFs"

Done.

3) line 86: "old radiation" → "old radiation scheme"

Done.

4) line 351: table 2 is referenced before table 1

Thank you for spotting this inconsistency. We rearranged the tables.

5) line 430: "adjust parameters target-oriented" → "adjust parameters in a target-oriented manner"

Done.

6) line 679: "much increased (decreased) to the radiative forcings" → "much increased (decreased) with respect to the radiative forcings"

We adjusted the sentence to "...much increased (decreased) in comparison to the radiative forcings...".

Reply to comments from Referee #2

(https://doi.org/10.5194/egusphere-2023-2140-RC2)

Below we will address all comments of referee #2 and will state corresponding changes in the manuscript. Again, we would like to thank referee #2 for taking the time to review our manuscript.

This manuscript describes major updates to the radiation schemes within the Modular Earth Submodel System (MESSy), which is an infrastructure designed to link different submodels into the same framework to more seamlessly perform simulations with different model components. Specifically, this work covers the implementation of the PSrad radiation scheme into MESSy, as well as updates to related submodels for calculating cloud optical properties (CLOUDOPT) and aerosol optical properties (AEROPT), as well as implementation into MESSy of a new albedo scheme (ALBEDO). The authors find that implementation of these schemes leads to reduced biases in temperature and humidity of a handful of key climate processes and improvement in radiative forcing variables for greenhouse gases relative to reference values. I find it particularly valuable that the implementation allows for easier calculation of radiative forcing through online double calls. These calculations are important but not routinely performed at most modeling centers. This manuscript is well written and will be of interest to GMD readers, especially as many modeling centers work towards updating their radiation schemes and, more generally, work towards stronger unification of submodels. I recommend some minor revisions detailed below.

We thank the reviewer for this rating of our manuscript. We will address all minor revisions suggested below.

General: I think readers would appreciate some information about computational performance when implementing the new radiative transfer scheme with more spectral bands. Was there a noticible increase in compute time with the new code and, if so, what steps did the developers take in an attempt to improve speeds?

We thank the reviewer for pointing out that this information was lacking in the manuscript. The computational time for the GCM-type simulation in-

creased by 70%, however this increase is due to the combined effect of the "old" vs the " new" setups, i.e. it includes also possible increases in computational time from the other updated submodels: AEROPT, CLOUDOPT, ALBEDO. For simulations with full chemistry, which we typically aim at, this increase will not play a major role due to the large computational demand of the chemistry solver. We have added a corresponding paragraph at the end of Section 3.1.: "Without additional diagnostic radiation calls for RF calculations as presented in Section 4, for a simulation performed on a single node[1] the computational time required for a radiation time step is around 70% higher for the PSrad setups than for the E5rad setups. If the full radiation calls are only performed every third time step (as in the simulation setups described above), this leads to an increase in the computational time of roughly 40%. This increase in computational time cannot be solely attributed to the core radiative transfer routines in RAD but is also affected by possible changes in computational time in the connected submodels AEROPT, CLOUDOPT and ALBEDO. To put this increase into perspective, we note that EMAC is commonly used in setups with comprehensive interactive chemistry (e.g. as chemistry-climate model). Due to the large computational demand of the chemistry solver the increase in computational time due to the radiation scheme will only be a fraction of the increase we report here for a GCM-type setup."
Footnote:"[1] 32 task on an AMD Epyc 7601 node with 32 cores"

Line 206-207: It may be a bit surprising to some, me included, that the developers decided to add a secondary LW ice mass extinction option that comes from a model that is now a few generations old (ECHAM4). What there a particularly reason to bring back this scheme? Some context here would be interesting.

We are sorry for the impression that we newly implemented this feature. It has been an option of the MESSy submodel CLOUDOPT before and we simply kept it for backward compatibility reasons. We slightly rephrased the sentence by changing "also allows" to "still allows" to make clear that this option was not introduced during our development but simply preserved.

Line 245-258: What is the role of this observational-based albedo climatology when the scheme is used to simulate climates beyond the present-day? Is the climatology used as a scaling factor to preserve seasonality? Is it only implemented for certain types of simulations?

Indeed the observational based albedo was not changed for our pi and pd simulations and it is not routinely implemented to use it to modify (transient) albedos associated with different climate states (e.g. concerning land-use change). However, we note that it is only the background albedo and is modified e.g. by the snow cover (see lines 268-275 in the discussion version). Before our implementations we have used an old background albedo from ECHAM5, which did not feature a seasonal cycle. Further, if a certain transient albedo associated with a specific scenario would be available, it could be easily applied with the new submodel ALBEDO (see lines 240-243 in the discussion version).

Section 2.6-1: Some motivation for providing additional flexibility in the orbital offset would be helpful. The previous version, where the offset would always falls in the middle between radiation calls, seems like the most reasonable approach for any case. Are there cases where another option is better? Some context would be helpful here.

We agree that some more motivation is needed. We have introduced the new option (middle between time steps associated with the respective radiation call), which we think is most suitable. We understand that referee #1 agrees on that. The previous option (middle between radiation steps) was preserved for backward compatibility. The freely adjustable option is important for offline radiation calculation purposes. In response to this comment and the comment by reviewer #1 (see minor comment 6) we adjusted the section as follows: "Now, the offset type can be selected via a new namelist switch. Apart from the previous choice $\Delta t_{orb,opt0}$, which we kept to ensure backward compatibility, the orbital parameters now can be chosen to be calculated for the middle of the interval of time steps associated with the current radiation call ($t_{r,i-1}$, $t_{r,i-1} + \Delta t_m$,..., $t_{r,i} - \Delta t_m$, leading to $\Delta t_{orb,opt1} = \frac{1}{2}((t_{r,i} - \Delta t_m) - t_{r,i-1})$, Fig. 2b), or the offset can be set to an arbitrary constant ($\Delta t_{orb,con} \leq \Delta t_r$). The latter option was introduced for offline radiation calculations."

Line 355: It is clear that the sets of simulations performed in this section have different radiation schemes (PSrad vs E5rad) but what about the modifications to the other relevant submodels discussed? I suspect the simulations using of PSrad also include all of the updates discussed for CLOUDOPT, AEROPT, ALBEDO and the orbital offset. If so, this should be noted in the text or better

incorporated into the experiment names for clarity.

We agree that the previous formulation at the beginning of Section 3.1 was not clear about this. Hence we adapted it: "We performed four simulations for the evaluation presented here. Namely, two simulations (pre-industrial and present-day denoted with pi and pd, respectively) for each of the two radiation schemes (the old ECHAM5 radiation scheme with the v2 in the SW, denoted here with E5rad, and the newly implemented PSrad scheme). These simulations will be addressed here as EMAC-E5rad-pi, EMAC-E5rad-pd, EMAC-PSrad-pi and EMAC-PSrad-pd, respectively. The simulation setups do not differ only in the radiation scheme but also according to the respective radiation scheme the typical old and new setups of AEROPT, CLOUDOPT and ALBEDO (as described before) have been chosen as indicated in Table 1. In all simulations the new choice for the orbital offset parameter (Δt_{orb}) was employed."
Information on the setup is partly also contained in Table 1 (previous Table 2). We now explicitly refer to this table and also adapted it such that the setups can be followed more easily.

General Section 3: The biases are presented clearly, and the authors focus on important ones, but I was hoping for some attempt to explain the causes of the bias, and particularly for situations where the e5rad and Psrad-driven simulation biases differ. Establishing causation is difficult in many cases, but some general discussion or potential explanations from the authors would be useful here. Is the warm stratosphere bias from the PSrad simulation (compared to the cold bias from the e5rads) related to the new handling of the orbital parameter offset, for instance?

We are glad that our comparison is presented clearly. We can also understand the wish to establish causality. However, from the simulations at hand this is difficult to do. We would need to setup additional experiments to disentangle the different effects due to changes of the albedo or the different tropospheric aerosol etc. We compare our results to the changes from ECHAM5 to ECHAM6 presented by Stevens et al. (2013), which are related to changes in the radiation scheme. But also in this study not only the radiation scheme was changed but at several instances the model was updated. However, we can rule out that the orbital parameter offset is causing this effect because the new choice for this parameter was used in all simulation that we present in the paper. Now we

mention this fact also in the text (see our reply to your previous question)

Also relevant to Figure 5: ERA5 has a known cold bias in stratospheric temperature from 2000 to 2006, The reanalysis was rerun for this period in a product called ERA5.1. I am unfamiliar with how large this bias was, but it would be interesting to see if the EMAC-PSrad bias is reduced for years outside of this range, or if ERA5.1 is used instead. Presumably the Figure 7 humidity bias is impacted too. Details here: `https://confluence.ecmwf.int/pages/viewpage.action?pageId=181130838`

We thank the reviewer for pointing this out. In the discussion version we did not add a note regarding ERA5.1 to avoid any confusion. In response to this comment, we decided to add the following paragraph after the comparison of specific humidity from ERA5 and our simulations: "Due to a setup inconsistency ERA5 has a cold bias in the stratosphere for the period 2000 to 2006, which also affects stratospheric water vapour (Simmons et al., 2020). This issue has been addressed in a new set of analyses called ERA5.1 covering this period (Simmons et al., 2020). We note however, that the differences between ERA5.1 and ERA5 regarding temperatures and water vapour as analysed by Simmons et al. (2020) are relatively small compared to the differences we see between ERA5 and our model simulations. Hence we simply applied the ERA5 data as the main conclusions regarding the model reanalyses differences will remain unchanged."

Line 599-606: Is the reduction in methane RF from IRF for PSrad significant? A 0.01 W/m2 reduction from IRF seems quite small and may just be noise, especially when the reduction does not appear to be present for the pi simulation. I mention this because although stratospheric adjustments related to SW absorption may be playing a role in a reduction, the Smith et al figure points to cloud adjustments playing in even larger role, an effect not being captured in this work. And recently, Allen et al. 2023 looked into the cooling from SW absorption of methane explicitly, finding much of it is driven by cloud adjustments, rather than a stratospheric adjustment: https://www.nature.com/articles/s41561-023-01144-z

We thank the reviewer for this comment. We have adjusted the respective section as follows: "Another aspect to note about the methane RFs is that

with E5rad the stratospheric temperature adjustment acts to increase the RF in comparison to the instantaneous RF, whereas for PSrad the differences between instantaneous and stratospheric adjusted RF are smaller and the sign depends on the background state. PSrad includes SW absorption of methane in two bands in the near-infrared (3.08 - 3.85 μm and 2.15 - 2.50 μm; cf. the RRTM bands described in the ECHAM6 documentation Giorgetta et al., 2013). The SW absorption acts to counteract the stratospheric cooling induced by the LW radiation (Byrom and Shine, 2022, their Fig. 2). Hence, the adjustment difference we find between PSrad and E5rad is in part consistent with the results from Smith et al. (2018, their Fig. S6). They point out that for the same experiments as analysed by Richardson et al. (2019), the rapid radiative adjustment induced by the stratospheric temperature adjustment is negative in models with the explicit treatment of methane SW absorption in the radiation scheme, and positive in models without. However, in the latter case the increase reported by Smith et al. (2018) is more pronounced as there is a substantial additional contribution from cloud radiative adjustments that are not covered by our technique."

Line 638-639: Yes, the Pincus pd background likely has a warmer surface thus CO2 forcing is stronger, but it also likely has a cooler stratosphere, which is arguably more impactful on CO2 forcing as highlighted by Jeevangee et al. 2021 and He et al. 2023. Related, this may explain why the CO2 forcing from the PSrad simulation is smaller than the E5rad simulations. PSrad produces a warmer stratosphere and thus the CO2 forcing is smaller.

Jeevangee et al. 2021: https://doi.org/10.1175/JCLI-D-19-0756.1

He et al. 2023: https://www.science.org/doi/10.1126/science.abq6872

We thank the reviewer for this comment. Regarding the impact of the stratosphere, we have adjusted the respective section: "(ii) In the climatological pd background, the tropospheric temperatures are likely higher and the stratospheric temperatures lower than for our pi background. Here, we reason that both changes will likely lead to an increased RF as diagnosed from CO_2-folding experiments, with the stratospheric component potentially making the larger contribution (He et al., 2023)"
Regarding the second part of the comment: We thank the reviewer for pointing this out. Indeed it seems that this could contribute to the differences. This can

be inferred from comparing our Table 6 with Table 8, where the latter shows all-sky instantaneous RFs when the radiation scheme is switched compared to the radiation scheme that drives the model simulation. Hence, we added a new paragraph after the introduction of Table 8: "Related to the dependence of RFs for CO_2 perturbations on the background, we have previously detected a larger CO_2 sensitivity in the E5rad compared to the PSrad simulations. As discussed above for the dependence of the instantaneous CO_2 RFs on the pi and pd background, we point out that a warmer stratosphere in the PSrad compared to the E5rad simulations might be contributing to the lower RF values diagnosed from PSrad compared to E5rad. In line with this argument, instantaneous all-sky CO_2 RFs increase (decrease) for E5rad (PSrad) when the background is provided by the switched radiation scheme PSrad (E5rad) as can be seen from the comparison of Tables 6 and 8."

References

R. E. Byrom and K. P. Shine. Methane's solar radiative forcing. *Geophysical Research Letters*, 49(15):e2022GL098270, 2022. doi: 10.1029/2022GL098270. URL https://agupubs.onlinelibrary.wiley.com/doi/abs/10.1029/2022GL098270.

R. R. Cordero, S. Feron, E. Sepúlveda, A. Damiani, J. M. Carrera, J. Jorquera, J. A. Alfonso, R. Fuenzalida, M. Rivas, S. MacDonell, G. Seckmeyer, C. Wang, Z. Ouyang, and S. Lhermitte. Evaluation of modis-derived estimates of the albedo over the atacama desert using ground-based spectral measurements. *Scientific Reports*, 11:19822, 2021. doi: 10.1038/s41598-021-98622-4. URL https://doi.org/10.1038/s41598-021-98622-4.

S. Dietmüller, P. Jöckel, H. Tost, M. Kunze, C. Gellhorn, S. Brinkop, C. Frömming, M. Ponater, B. Steil, A. Lauer, and J. Hendricks. A new radiation infrastructure for the modular earth submodel system (messy, based on version 2.51). *Geoscientific Model Development*, 9(6):2209–2222, 2016. doi: 10.5194/gmd-9-2209-2016. URL https://gmd.copernicus.org/articles/9/2209/2016/.

M. Etminan, G. Myhre, E. J. Highwood, and K. P. Shine. Radiative forcing of carbon dioxide, methane, and nitrous oxide: A significant revision of the methane radiative forcing. *Geophysical Research Letters*, 43(24): 12,614–12,623, 2016. doi: 10.1002/2016GL071930. URL https://agupubs.onlinelibrary.wiley.com/doi/abs/10.1002/2016GL071930.

M. A. Giorgetta, E. Roeckner, T. Mauritsen, J. Bader, T. Crueger, M. Esch, S. Rast, L. Kornblueh, H. Schmidt, S. Kinne, C. Hohenegger, B. Möbis, T. Krismer, K. Wieners, and B. Stevens. The atmospheric general circulation model ECHAM6 - Model description. *Reports on Earth System Science / Max-Planck-Institut für Meteorologie*, 135, 2013. doi: 10.17617/2.1810480.

M. A. Giorgetta, R. Brokopf, T. Crueger, M. Esch, S. Fiedler, J. Helmert, C. Hohenegger, L. Kornblueh, M. Köhler, E. Manzini, T. Mauritsen, C. Nam, T. Raddatz, S. Rast, D. Reinert, M. Sakradzija, H. Schmidt, R. Schneck, R. Schnur, L. Silvers, H. Wan, G. Zängl, and B. Stevens. Icon-a, the atmosphere component of the icon earth system model: I. model description. *Journal of Advances in Modeling Earth Systems*, 10(7):1613–1637,

2018. doi: 10.1029/2017MS001242. URL https://agupubs.onlinelibrary.wiley.com/doi/abs/10.1029/2017MS001242.

H. He, R. J. Kramer, B. J. Soden, and N. Jeevanjee. State dependence of co_2 forcing and its implications for climate sensitivity. *Science*, 382(6674):1051–1056, 2023. doi: 10.1126/science.abq6872. URL https://www.science.org/doi/abs/10.1126/science.abq6872.

P. Jöckel, H. Tost, A. Pozzer, M. Kunze, O. Kirner, C. A. M. Brenninkmeijer, S. Brinkop, D. S. Cai, C. Dyroff, J. Eckstein, F. Frank, H. Garny, K.-D. Gottschaldt, P. Graf, V. Grewe, A. Kerkweg, B. Kern, S. Matthes, M. Mertens, S. Meul, M. Neumaier, M. Nützel, S. Oberländer-Hayn, R. Ruhnke, T. Runde, R. Sander, D. Scharffe, and A. Zahn. Earth System Chemistry integrated Modelling (ESCiMo) with the Modular Earth Submodel System (MESSy) version 2.51. *Geoscientific Model Development*, 9 (3):1153–1200, 2016. doi: 10.5194/gmd-9-1153-2016. URL http://www.geosci-model-dev.net/9/1153/2016/.

Z. Li, A. Erb, Q. Sun, Y. Liu, Y. Shuai, Z. Wang, P. Boucher, and C. Schaaf. Preliminary assessment of 20-m surface albedo retrievals from sentinel-2a surface reflectance and modis/viirs surface anisotropy measures. *Remote Sensing of Environment*, 217:352–365, 2018. ISSN 0034-4257. doi: 10.1016/j.rse.2018.08.025. URL https://www.sciencedirect.com/science/article/pii/S0034425718304024.

J. Liu, C. Schaaf, A. Strahler, Z. Jiao, Y. Shuai, Q. Zhang, M. Roman, J. A. Augustine, and E. G. Dutton. Validation of moderate resolution imaging spectroradiometer (modis) albedo retrieval algorithm: Dependence of albedo on solar zenith angle. *Journal of Geophysical Research: Atmospheres*, 114(D1), 2009. doi: 10.1029/2008JD009969. URL https://agupubs.onlinelibrary.wiley.com/doi/abs/10.1029/2008JD009969.

M. Meinshausen, E. Vogel, A. Nauels, K. Lorbacher, N. Meinshausen, D. M. Etheridge, P. J. Fraser, S. A. Montzka, P. J. Rayner, C. M. Trudinger, P. B. Krummel, U. Beyerle, J. G. Canadell, J. S. Daniel, I. G. Enting, R. M. Law, C. R. Lunder, S. O'Doherty, R. G. Prinn, S. Reimann, M. Rubino, G. J. M. Velders, M. K. Vollmer, R. H. J. Wang, and R. Weiss. Historical greenhouse gas concentrations for climate modelling (cmip6). *Geoscientific Model Development*, 10(5):2057–2116, 2017. doi: 10.5194/gmd-10-2057-2017. URL https://gmd.copernicus.org/articles/10/2057/2017/.

G. Myhre, E. J. Highwood, K. P. Shine, and F. Stordal. New estimates of radiative forcing due to well mixed greenhouse gases. *Geophysical Research Letters*, 25(14):2715–2718, July 1998. doi: 10.1029/98GL01908.

R. Pincus and B. Stevens. Paths to accuracy for radiation parameterizations in atmospheric models. *Journal of Advances in Modeling Earth Systems*, 5(2):225–233, 2013. doi: 10.1002/jame.20027. URL `https://agupubs.onlinelibrary.wiley.com/doi/abs/10.1002/jame.20027`.

R. Pincus, S. A. Buehler, M. Brath, C. Crevoisier, O. Jamil, K. Franklin Evans, J. Manners, R. L. Menzel, E. J. Mlawer, D. Paynter, R. L. Pernak, and Y. Tellier. Benchmark calculations of radiative forcing by greenhouse gases. *Journal of Geophysical Research: Atmospheres*, 125 (23):e2020JD033483, 2020. doi: 10.1029/2020JD033483. URL `https://agupubs.onlinelibrary.wiley.com/doi/abs/10.1029/2020JD033483`. e2020JD033483 10.1029/2020JD033483.

T. B. Richardson, P. M. Forster, C. J. Smith, A. C. Maycock, T. Wood, T. Andrews, O. Boucher, G. Faluvegi, D. Fläschner, Hodnebrog, M. Kasoar, A. Kirkevåg, J.-F. Lamarque, J. Mülmenstädt, G. Myhre, D. Olivié, R. W. Portmann, B. H. Samset, D. Shawki, D. Shindell, P. Stier, T. Takemura, A. Voulgarakis, and D. Watson-Parris. Efficacy of climate forcings in pdrmip models. *Journal of Geophysical Research: Atmospheres*, 124(23): 12824–12844, 2019. doi: 10.1029/2019JD030581. URL `https://agupubs.onlinelibrary.wiley.com/doi/abs/10.1029/2019JD030581`.

E. Roeckner, G. Bäumel, L. Bonaventura, R. Brokopf, M. Esch, M. Giorgetta, S. Hagemann, I. Kirchner, L. Kornblueh, E. Manzini, A. Rhodin, U. Schlese, U. Schulzweida, and A. Tompkins. The atmospheric general circulation model ECHAM5, PART I, Model description. *Report / Max-Planck-Institut für Meteorologie*, 349, 2003. doi: 10.17617/2.995269.

A. Simmons, C. Soci, J. Nicolas, B. Bell, P. Berrisford, R. Dragani, J. Flemming, L. Haimberger, S. Healy, H. Hersbach, A. Horányi, A. Inness, J. Munoz-Sabater, R. Radu, and D. Schepers. Global stratospheric temperature bias and other stratospheric aspects of era5 and era5.1, 01/2020 2020. URL `https://www.ecmwf.int/node/19362`.

C. J. Smith, R. J. Kramer, G. Myhre, P. M. Forster, B. J. Soden, T. Andrews, O. Boucher, G. Faluvegi, D. Fläschner, Hodnebrog, M. Kasoar, V. Kharin,

A. Kirkevåg, J.-F. Lamarque, J. Mülmenstädt, D. Olivié, T. Richardson, B. H. Samset, D. Shindell, P. Stier, T. Takemura, A. Voulgarakis, and D. Watson-Parris. Understanding rapid adjustments to diverse forcing agents. *Geophysical Research Letters*, 45(21):12,023–12,031, 2018. doi: 10.1029/2018GL079826. URL https://agupubs.onlinelibrary.wiley.com/doi/abs/10.1029/2018GL079826.

L. Stecher, F. Winterstein, M. Dameris, P. Jöckel, M. Ponater, and M. Kunze. Slow feedbacks resulting from strongly enhanced atmospheric methane mixing ratios in a chemistry–climate model with mixed-layer ocean. *Atmospheric Chemistry and Physics*, 21(2):731–754, 2021. doi: 10.5194/acp-21-731-2021. URL https://acp.copernicus.org/articles/21/731/2021/.

B. Stevens, M. Giorgetta, M. Esch, T. Mauritsen, T. Crueger, S. Rast, M. Salzmann, H. Schmidt, J. Bader, K. Block, R. Brokopf, I. Fast, S. Kinne, L. Kornblueh, U. Lohmann, R. Pincus, T. Reichler, and E. Roeckner. Atmospheric component of the mpi-m earth system model: Echam6. *Journal of Advances in Modeling Earth Systems*, 5(2):146–172, 2013. doi: 10.1002/jame.20015. URL https://agupubs.onlinelibrary.wiley.com/doi/abs/10.1002/jame.20015.

N. Stuber, R. Sausen, and M. Ponater. Stratosphere adjusted radiative forcing calculations in a comprehensive climate model. *Theoretical and Applied Climatology*, 68:125–135, 2001. doi: 10.1007/s007040170041. URL https://doi.org/10.1007/s007040170041.

F. Winterstein, F. Tanalski, P. Jöckel, M. Dameris, and M. Ponater. Implication of strongly increased atmospheric methane concentrations for chemistry–climate connections. *Atmospheric Chemistry and Physics*, 19 (10):7151–7163, 2019. doi: 10.5194/acp-19-7151-2019. URL https://www.atmos-chem-phys.net/19/7151/2019/.

Updating the radiation infrastructure in MESSy (based on MESSy version 2.55)

Matthias Nützel[1,a], Laura Stecher[1], Patrick Jöckel[1], Franziska Winterstein[1], Martin Dameris[1], Michael Ponater[1], Phoebe Graf[b], and Markus Kunze[2]

[1]Deutsches Zentrum für Luft- und Raumfahrt, Institut für Physik der Atmosphäre, Oberpfaffenhofen, Germany
[2]Leibniz Institute of Atmospheric Physics (IAP), Kühlungsborn, Germany
[a]now at: Meteorologisches Institut München, Ludwig-Maximilians-Universität München, Munich, Germany
[b]previously at: [1]

Correspondence: Matthias Nützel (matthias.nuetzel@dlr.de)

Abstract.

The calculation of the radiative transfer is a key component of global circulation models. In this manuscript we describe the most recent updates of the radiation infrastructure in the Modular Earth Submodel System (MESSy). These updates include the implementation of the PSrad radiation scheme within the RAD submodel. Further, the radiation-related submodels CLOUDOPT (for the calculation of cloud optical properties) and AEROPT (for the calculation of aerosol optical properties) have been updated and are now more flexible in order to deal with different sets of shortwave and longwave bands of radiation schemes. In the wake of these updates a new submodel (ALBEDO), which features solar zenith angle dependent albedos and a new satellite-based background (white-sky) albedo, was created. All of these developments are backward compatible and previous features of the MESSy radiation infrastructure remain available. Moreover, these developments mark an important step in the use of the ECHAM/MESSy Atmospheric Chemistry (EMAC) model as the update of the radiation scheme was a key aspect in the development of the sixth generation of the ~~the~~ European Centre for Medium-Range Weather Forecasts – HAMburg (ECHAM6) model from ECHAM5~~and they~~. The developments presented here also aim towards the use of ~~MESSy~~ the MESSy infrastructure with the ICOsahedral Non-hydrostatic (ICON) model as a base model. The improved infrastructure will also aid in the implementation of additional radiation schemes once this should be needed.

We have optimized the set of free parameters for two ~~dynamical model~~ general circulation model-type (GCM-type) setups for pre-industrial and present-day conditions: one with the radiation scheme that was used up to date (i.e. the radiation scheme of ECHAM5) and one with the newly implemented PSrad radiation scheme. After this parameter optimization, we performed four model simulations and evaluated the corresponding model results using reanalysis and observational data. The most apparent improvements related to the updated radiation scheme are the reduced cold biases in the tropical upper troposphere and lower stratosphere and the extratropical lower stratosphere, and a strengthened polar vortex. The former is also related to improved stratospheric humidity and its variability if the new radiation scheme is employed.

Using the multiple radiation call capability of MESSy, we have applied the two model configurations to calculate instantaneous and stratospheric adjusted radiative forcings related to changes in greenhouse gases. Overall, we find that for many forcing experiments the simulations with the new radiation scheme show improved radiative forcing values. This is in particular the case for methane radiative forcings, which are considerably higher when ~~asessed~~ assessed with the new radiation scheme and thus in better agreement with reference values.

1 Introduction

The most accurate models for calculating the radiative transfer within the atmosphere are line-by-line (LBL) models (e.g. Pincus et al., 2015). Results from radiative transfer calculations with these models agree well with observations (e.g. Oreopoulos and Mlawer, 2010; Oreopoulos et al., 2012; Pincus et al., 2015, and references therein). The shortwave (SW) and longwave (LW) broad band errors of LBL models are in the order of $1\,\mathrm{W\,m^{-2}}$ (Pincus et al., 2015, and references therein). However, these detailed radiative transfer models are computationally too expensive to be run in global climate models (e.g. Oreopoulos et al., 2012). Hence, in global climate models the radiative transfer calculation is simplified compared to LBL models (e.g. Oreopoulos et al., 2012) and it is also, typically, not performed every time step (Pincus and Stevens, 2013). In total, there is the challenge for these simplified radiative transfer codes to be sufficiently precise and efficient (Pincus and Stevens, 2013). This causes the need to revise the radiation schemes which are employed in global models from time to time.

Here, we describe how we extended the Modular Earth Submodel System (MESSy; Jöckel et al., 2005, 2010) infrastructure to include the PSrad radiation scheme (Pincus and Stevens, 2013) for further use in MESSy-based climate simulations. The previous status of the MESSy radiation infrastructure is evident from Dietmüller et al. (2016). They document how the radiation infrastructure of the fifth generation European Centre for Medium-Range Weather Forecasts – HAMburg (Roeckner et al., 2003, 2006, ECHAM5;) model was restructured to be "MESSy-fied", i.e. to be modularized according to the MESSy coding standard: new (MESSy) submodels have been created from code parts of the radiation calculation which are related to, but to a certain degree independent of, the radiation scheme. These new submodels were (i) AEROPT for the provision of aerosol optical properties, (ii) CLOUDOPT for the calculation of cloud optical properties and (iii) ORBIT to determine the orbital parameters, which are needed e.g. for the calculation of the radiative transfer. During this process also the structure of the radiation scheme was "MESSy-fied" and the corresponding MESSy submodel RAD was created.

Besides the pure modularization, Dietmüller et al. (2016) also describe that the MESSy radiation infrastructure provides additional valuable features connected to the radiation calculation. One example is the possibility for multiple (diagnostic) calls of AEROPT, CLOUDOPT and RAD, which can be used to determine multiple instantaneous radiative forcings (RFs) or

stratospheric adjusted ~~radiative~~ RFs (as described by Stuber et al., 2001) online in a single simulation (see e.g. Hansen et al., 2005, for a definition of instantaneous and adjusted RFs). This is a powerful feature as the need for extensive output, which would be required for an offline (post-simulation) calculation, is avoided and (if intended) all calculations are consistently performed with exactly the same version of the radiation scheme. Further, the diagnostic calls are performed under the same meteorological conditions and at the highest possible frequency, i.e. the frequency of the radiation calls. Hence, a major concern during the development phase, which is described here, was to secure backward compatibility (up to the degree of binary identity to some point) and the possibility of retaining these features in connection with the newly added radiation scheme. Besides the integration of an additional radiation scheme, we also made the radiation infrastructure more flexible. Moreover, we created the MESSy submodel ALBEDO, which now contains the previous code for the calculation of the surface albedo extracted from the RAD submodel and newly added parametrizations for the calculation of the surface albedo.

As mentioned above, until now the default radiation scheme in MESSy was a modularized version of the ECHAM5 radiation scheme, which we will denote by E5rad throughout this paper. For many years the Max Planck Institute for Meteorology (MPI-M) in Hamburg, Germany, has developed the general circulation model ECHAM (e.g. Roeckner et al., 1996, 2003; Stevens et al., 2013). An important step from the fifth generation of ECHAM to ECHAM6.1 was an update concerning the radiation scheme, in particular as in the SW the number of bands was increased from 4 to 14 (Stevens et al., 2013). For the latest version of ECHAM, ECHAM6.3, the LW and SW radiation parametrization was once more revised as the PSrad scheme (Pincus and Stevens, 2013) was made available (Giorgetta et al., 2018; Mauritsen et al., 2019). This version of ECHAM - with PSrad as the radiation model - also constitutes the atmospheric component of MPI-ESM1.2, the MPI-M's Earth System Model, which is described by Mauritsen et al. (2019). Simulations with MPI-ESM1.2 have contributed to the most recent phase of the coupled model intercomparison project (CMIP6; Eyring et al., 2016, see https://pcmdi.llnl.gov/CMIP6/ArchiveStatistics/esgf_data_holdings/, accessed last 10 Jul 2023, for a list of available model output).

Similarly, PSrad is the radiation scheme employed in an ICOsahedral Non-hydrostatic (ICON originally developed by the Deutscher Wetterdienst, DWD, and the MPI-M Zängl et al., 2015) model version described by Giorgetta et al. (2018). We decided to add the PSrad scheme (as implemented in ICON version 2.4.0) to the radiation schemes, which are available within the MESSy infrastructure. This update marks an important step to incorporate previous model developments of the ECHAM family within the MESSy infrastructure, while it is also an important step towards the use of ICON as a base model within the MESSy infrastructure.

Further, we expect a reduction or removal of previous shortcomings related to the old radiation scheme when employing the new radiation scheme PSrad in ECHAM/MESSy Atmospheric Chemistry (EMAC) simulations. For example, previous studies with EMAC and the ECHAM5 radiation scheme have shown considerably low radiative effects for methane. For instance, a doubling of the present-day reference value for methane of $1.8\,\mu\mathrm{mol\,mol}^{-1}$ resulted in a top-of-atmosphere stratospheric

adjusted RF of 0.23 W m^{-2} (Winterstein et al., 2019; Stecher et al., 2021), while studies of Myhre et al. (1998) and Etminan et al. (2016) suggest 0.53 W m^{-2} and 0.62 W m^{-2}, respectively, for doubling of the reference value of 1.7 μmol mol^{-1}.

In the following, we present the recent developments concerning the radiation-related MESSy submodels, AEROPT, CLOUDOPT, RAD and the new MESSy submodel ALBEDO (Sect. 2). The ~~dynamic~~ GCM-type atmosphere-only model setups (i.e. no interactive aerosol, only simplified methane chemistry) driven either by the new (PSrad) or the old (ECHAM5) radiation scheme, as well as the parameter optimization process are presented in Sect. 3. This section also features the evaluation of these model setups with observational and reanalysis data. In Sect. 4 we show RF estimates derived using the old and new radiation scheme and we compare our results to results from previous studies (Sect. 4). Finally, we close with a summary of the presented results (Sect. 5).

2 Radiation infrastructure updates

2.1 MESSy (short description)

Here, we describe the updates of the radiation infrastructure of the Modular Earth Submodel System (MESSy; Jöckel et al., 2005, 2010), which are now implemented in MESSy based on version 2.55. MESSy is a middleware to link different submodels (e.g. representing physical processes, chemical processes, online diagnostics, or external couplers) with a base (dynamical core) model. The key concept behind MESSy is that it provides the general infrastructure to perform simulations with a specific base model and clean interfaces, which allow the coupling of different submodels to this base model (Jöckel et al., 2005) or even the internal coupling of different modelling compartments (Pozzer et al., 2011). The software layers to ensure this clear separation are the base model layer (BML) and base model interface layer (BMIL), which contain the base model's code and the interface to connect submodels to the base model, respectively (Jöckel et al., 2005). Similarly, submodels are split into two layers, which contain the core of the submodels computations in the submodel core layer (SMCL) and the submodel interface layer (SMIL) to connect with other submodels or the BMIL (Jöckel et al., 2005). The exchange of variables (between submodels etc.) is handled via the "CHANNEL" interface (Jöckel et al., 2010) to avoid compile time dependencies between the core routines of different submodels.

Dietmüller et al. (2016) describe the state of the MESSy radiation infrastructure at the starting point of our new implementations. With the radiation infrastructure update and development of the submodels AEROPT, CLOUDOPT, RAD and ORBIT, they made a big step towards a clean separation between (i) code components that are relevant for the radiation calculation but which can be separated, from a software development perspective, from the core radiative transfer model and (ii) the core radiative transfer model. Of course, it must be still ensured that the input and output variables of the submodels connect properly: for example, if the SW scheme has a set of bands, AEROPT and CLOUDOPT must provide aerosol and cloud optical properties for exactly those bands. Consequently, with the introduction of an additional radiation scheme, we had to update the submodels AEROPT and CLOUDOPT as the band structure of the newly added radiation scheme, PSrad, differs from the old

one (see Sect. 2.2). Further, we conducted an additional separation of code that is independent of the core radiation calculation by creating the new MESSy submodel ALBEDO for the calculation of the surface albedo, which is then provided as an input for the radiation scheme. A key requirement of the updates was to preserve the previous flexibility, in particular concerning the application of multiple calls of the radiation scheme as well as multiple calls of the aerosol and cloud optical schemes, as described by Dietmüller et al. (2016). Figure 1 gives an overview of the new radiation infrastructure. The following sections describe the updates for each of the radiation infrastructure submodels (i.e. all submodels that are directly related to calling the radiation scheme) in MESSy in comparison to the state described by Dietmüller et al. (2016). The described changes are available at the latest in ALBEDO version 1.4, AEROPT version 2.1.0, CLOUDOPT version 2.5 and RAD 3.0.

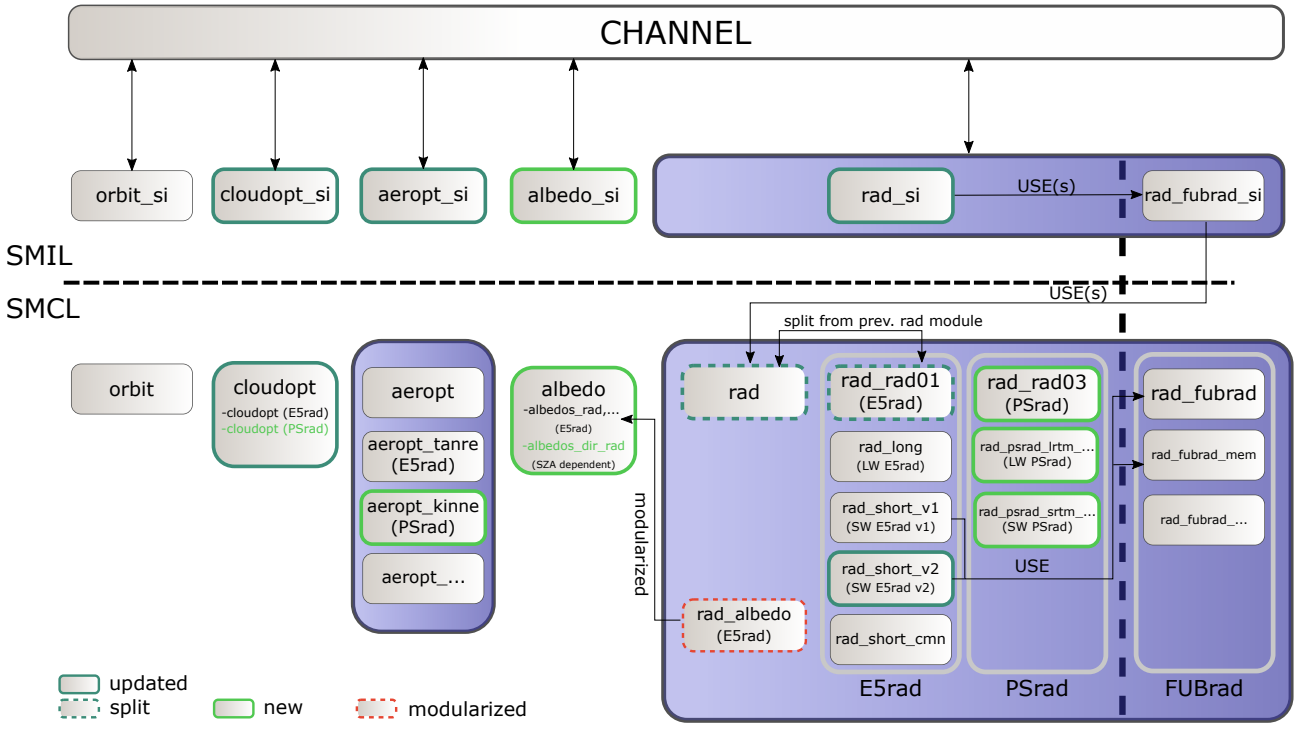

Figure 1. Schematic overview of the updated MESSy radiation infrastructure in comparison to the state described by Dietmüller et al. (2016; see also their Fig. 1). Green colour indicates new submodels (either Fortran modules or Fortran subroutines). Individual Fortran modules are shown as grey boxes. If the MESSy submodels encompass more than one Fortran module this is indicated via blueish boxes. See text for details. In addition to the depicted changes, additional minor modifications, e.g. in the AEROPT core layer modules, have been made during the revision of the radiation infrastructure.

2.2 RAD: updates of the MESSy radiation submodel

The submodel RAD calculates the radiative transfer taking into account aerosols, clouds, and selected gaseous species relevant for radiative transfer (Dietmüller et al., 2016). Based on Dietmüller et al. (2016), we give the following recap of the RAD submodel before our implementation: In RAD a MESSy-fied version of the ECHAM5 radiation scheme is available. This module comprises a LW radiation scheme with 16 bands (RRTM; Mlawer et al., 1997) and two SW schemes (short_v1 and short_v2) with four bands each, both based on Fouquart and Bonnel (1980), whereas short_v2 includes the improvements of Thomas (2008). The MESSy submodel FUBrad (Nissen et al., 2007; Kunze et al., 2014) can be switched on to overcome the relatively coarse resolution in the SW, which allows for high-resolution UV radiative transfer calculations in the stratosphere above 70 hPa, and extends the spectral range by including O_2 UV absorption in the Schumann-Runge bands/continuum and Lyman-α.

Here, we implemented the radiation scheme PSrad (Pincus and Stevens, 2013), as available in ICON version 2.4.0, into the MESSy submodel RAD. As described by Pincus and Stevens (2013), the development of PSrad was guided by RRTMG (Mlawer et al., 1997; Iacono et al., 2008). RRTMG in turn features 16 bands in the LW and 14 bands in the SW (Iacono et al., 2008; see also Tables 2.3 and 2.4 presented by Giorgetta et al., 2013b, for the band structure). To make the PSrad scheme available alongside the "old" schemes, we introduce a new software "layer" in the MESSy RAD submodel core by splitting the previous core module "messy_rad.f90" into two new Fortran modules "messy_rad.f90" and "messy_rad_rad01.f90", where the latter contains all subroutines from the previous "messy_rad.f90" directly related to the ECHAM5 radiation scheme(s). In analogy to "messy_rad_rad01.f90" for the old radiation scheme, "messy_rad_rad03.f90" provides the interface to the new radiation scheme (PSrad). The Fortran module was numbered with "rad03" as in the SW rad01 already contains 2 schemes rad_short_v1 and rad_short_v2. In principle, the two LW and three SW schemes can be combined freely and the introduction of additional schemes should be straightforward, if they are well modularized. However, for new combinations additional parameter optimization (see Sect. 3.2) will likely be required. While it is still possible to use FUBrad with the old SW radiation schemes, this is not yet possible with the new SW scheme. In a future step, also the new SW scheme is envisaged to be available in combination with the FUBrad submodel. At the moment, however, the model terminates with a controlled shutdown and a corresponding error message, if this combination is selected.

This implementation marks a major update of EMAC as one key update between ECHAM5 and ECHAM6 was the update of the (SW) radiation scheme (Stevens et al., 2013), which in ECHAM6.3 was updated to PSrad (Giorgetta et al., 2018; Mauritsen et al., 2019). Further, it also marks an important step for the transition towards ICON as a MESSy base model as we implemented PSrad as available in the ICON version described by Giorgetta et al. (2018).

In addition to the distribution of greenhouse gases (GHGs) and meteorological data, the radiation scheme requires input regarding cloud optical properties, aerosol optical properties and the surface albedo (see e.g. Dietmüller et al., 2016). For a

typical simulation this information now comes from the MESSy submodels CLOUDOPT, AEROPT and the new submodel ALBEDO. Below, we describe for such a typical simulation how these radiation-related submodels (or previous Fortran routines in the case of ALBEDO) have been modified during the revision of the radiation infrastructure. However, we note that it is also possible to feed the respective input, e.g. from a previous simulation, into the RAD submodel via the MESSy submodel IMPORT (Kerkweg and Jöckel, 2015), which allows among others to read time series of gridded data from netcdf files.

2.3 AEROPT: updates of the MESSy submodel for the calculation of aerosol optical properties

The AEROPT submodel (Dietmüller et al., 2016) calculates the aerosol optical properties that are required for the radiative transfer calculation in the RAD submodel, namely: aerosol optical depth for the LW and SW, and single scattering albedo and asymmetry factor for the SW only, as scattering in the LW is neither considered in E5rad (Roeckner et al., 2003), nor in PSrad (Pincus and Stevens, 2013). These optical properties are wavelength dependent. As the number of SW bands is different for PSrad compared to the old (ECHAM5) radiation scheme, the AEROPT submodel had to be revised. Consequently, the number of wavelength bands can vary between different sets of aerosol optical properties. We achieve this, as now for each call the AEROPT submodel provides CHANNEL objects with the corresponding number of wavelength bands.

Further, the Max-Planck-Institute Aerosol Climatology version 1 (MACv1) for tropospheric aerosol optical properties described by Kinne et al. (2013) was made available via IMPORT and by introducing an ICON (version 2.4.0) routine (new MESSy Fortran module "messy_aeropt_kinne.f90"), which maps the aerosol optical properties to the model's current height profile and merges the climatologies for fine and coarse mode aerosol in the SW ~~(see Giorgetta et al., 2013a, for the mapping and merging d~~ (see Giorgetta et al., 2013b, for the mapping and merging details).

All other features of the AEROPT submodel as described by Dietmüller et al. (2016) remain fully functional, e.g. multiple diagnostic calls of the AEROPT submodel or the combination of different aerosol sets. The latter is typically used to merge tropospheric and stratospheric aerosol data and while merging, the consistency of the number of wavelength bands is checked. While it is still available for the old radiation scheme, the coupling of online calculated aerosol is not yet implemented for the PSrad scheme. However, this functionality is ~~supposed to follow~~ due to be implemented with a revision of the AEROPT submodel.

2.4 CLOUDOPT: updates of the MESSy submodel for the calculation of cloud optical properties

The submodel CLOUDOPT (Dietmüller et al., 2016) provides the cloud optical properties, which are needed for the calculation of the radiation in the submodel RAD. So far, in analogy to the aerosol optical properties provided by AEROPT, CLOUDOPT provides the band-dependent cloud optical properties of optical depth (again for LW and SW), single scattering albedo (SW) and asymmetry factor (SW). We revised the CLOUDOPT submodel to account for the band structure of the new radiation scheme. CLOUDOPT now also contains the calculation of cloud optical properties, as described by Stevens et al. (2013) and

implemented in ICON (version 2.4.0). As for the AEROPT submodel, we generalized the infrastructure. Now, the number of wavelength bands of the CHANNEL objects can vary with each call of the CLOUDOPT submodel. Together with the adaptions in AEROPT, this allows to call radiation schemes with different spectral resolutions within a single simulation for diagnostic purposes.

In the LW the mass extinction coefficients of the new scheme follow the ECHAM5 parametrizations (Stevens et al., 2013), which were presented by Roeckner et al. (2003). For liquid clouds the relation between effective radii and mass extinction is given in equations 8 and 11.61 of Stevens et al. (2013) and Roeckner et al. (2003), respectively. For ice clouds, the parametrization is based on Ebert and Curry (1992; see Roeckner et al., 2003; Stevens et al., 2013). In addition, CLOUDOPT ~~also~~ still allows the use of an alternative calculation for ice mass extinction in the LW, which was adopted from ECHAM4 (Eq. 101 and Table 3 of Roeckner et al., 1996). For the SW the new scheme derives the mass extinction, single scattering albedo and asymmetry factors from look-up tables (Stevens et al., 2013), whereas the old scheme uses a set of coefficients to derive SW optical properties from effective radii (Roeckner et al., 2003).

As in ECHAM5 and ECHAM6, the cloud optical depths of liquid and ice clouds are rescaled using a cloud inhomogeneity factor to account for the subgrid-scale variability of clouds (Roeckner et al., 2003; Mauritsen et al., 2012; Stevens et al., 2013; Mauritsen et al., 2019; Mauritsen and Roeckner, 2020, see keywords "zinhoml" and "zinhomi" in the supporting information of the latter). For liquid clouds, the inhomogeneity factors can now be set depending on the cloud type (convection type). In the namelist three inhomogeneity factors can be set for convection-free, convective and certain shallow convective clouds (see Mauritsen et al., 2019; Mauritsen and Roeckner, 2020, supporting information of the latter) in analogy to the implementation in ECHAM6.3 and ICON.

In CLOUDOPT and in the radiation schemes the (default) cloud overlap is assumed to be maximum-random overlap (Roeckner et al., 2003; Dietmüller et al., 2016; Giorgetta et al., 2018). In the case of PSrad the overlap assumption is treated based on the Monte Carlo Independent Column Approximation (McICA) technique (see Giorgetta et al., 2018, for details and further refere

.

2.5 ALBEDO: introduction of the new MESSy submodel for the calculation of surface albedos

As a final step to separate code from the RAD submodel that is independent of the radiation scheme, the calculation of the surface albedo was modularized. Therefore, we introduced the new submodel ALBEDO. This new MESSy submodel contains the previous (ECHAM5-based) routines to calculate the surface albedo and was extended by adding new parametrizations and additional features for the calculation of solar zenith angle (SZA) dependent surface albedos. In particular, ALBEDO ~~can calculate~~ calculates a blue-sky albedo (α_{blue}) from the black-sky (α_{black}) and white-sky ~~albedos~~ albedo (α_{white}) and the fraction of direct and diffuse ~~surface radiation fluxes (see e.g. ?Liu et al., 2009; Cordero et al., 2021, and references therein for details on the different albed~~

-radiation fluxes with respect to the total downwelling shortwave fluxes at the surface ($f^{dir}_{sw,surf}$, $f^{dif}_{sw,surf}$) as $\alpha_{blue} = f^{dir}_{sw,surf}\,\alpha_{black} + f^{dif}_{sw,surf}\,\alpha_{white}$ (see e.g. Liu et al., 2009; Li et al., 2018; Cordero et al., 2021, and references therein for details on the different albedos and how to typical
235 . Here, the black-sky albedo relates to the albedo associated with the collimated beam, whereas the white-sky albedo corresponds to the albedo associated with isotropic diffuse radiation (Liu et al., 2009). Further details on the modularization and updates are described below.

ECHAM5 (background) albedo

240 ECHAM5 uses a so-called background albedo for snow-free land surfaces (Roeckner et al., 2003). This temporally constant (i.e., without interannual or subseasonal variation) climatological field is based on Hagemann (2002). This background albedo is modified according to meteorological and land properties and an albedo for grid points containing sea ice is calculated (Roeckner et al., 2003). Finally, the resulting fields are combined with a constant value for the albedo of ice-free ocean surfaces to produce the final (blue-sky) albedo, employed in the ECHAM5 model (Roeckner et al., 2003). The corresponding routine is
245 shifted to the core layer of the new ALBEDO submodel and is called from the respective submodel interface layer.

New white-sky albedo for snow-free land

Here, we introduce a new white-sky albedo for snow-free land surfaces, which can be used to calculate SZA dependent surface albedos and is practically a substitute for the previous ECHAM5 background albedo. This white-sky albedo is a monthly mean climatology based on data from the Moderate Resolution Imaging Spectroradiometer (MODIS; https://modis.gsfc.nasa.gov/
250 about/ accessed last 03 February 2023). Furthermore, in principle, it is possible to use any (background or white-sky) albedo with any temporal resolution as input via IMPORT, since the (background or white-sky) albedo is now namelist controlled. So, besides the newly added monthly climatology with subseasonal variation also other albedo data with different variability (e.g. transient) could be fed in as background albedo via IMPORT.

255 The provided white-sky albedo was produced from the MODIS/Terra+Aqua BRDF/Albedo Gap-Filled Snow-Free Daily L3 Global 30ArcSec CMG V006 data product (MCD43GFv006; Sun et al., 2017; Schaaf, 2019). We used the white-sky albedo near shortwave broadband and the period from 01 January 2001 to 31 December 2010. The original data are daily files on a 43200 x 21600 grid. This grid corresponds roughly to a pixel size of 1 km x 1 km. Values of the white-sky albedo below 0.07 in the raw daily files are set to missing (guided by the reference value for the ocean surface albedo used in ECHAM5;
260 Roeckner et al., 2003) and the resulting files are further used to calculate monthly means. We calculate a climatology over all months, which we use to fill in missing values in the original monthly mean files: i.e. we substitute missing values in the original monthly files with a climatological value calculated from the original monthly files where the particular pixel is not missing. Consequently, a 12-month climatology is calculated from the collection of the updated monthly files. The all-time climatology is used to create common generic conversion weights to remap both climatologies (all time and 12 months) to a
265 360×180 grid. ~~Still~~ Any remaining missing grid points in the two climatological files - which can occur as there might be

grid points which are missing in all months, which were used to calculate the climatology - are filled using a nearest neighbour method. This procedure ensures that when the resolution-dependent land mask is applied in a simulation, the white-sky albedo for snow-free land includes land albedo values only.

Solar zenith angle dependent albedo

One main aspect during the modularization of the ALBEDO submodel was to include the SZA dependence of the albedo for water, land and snow. For the SZA dependence of the ocean surface, the parametrization as described in Appendix A of Li et al. (2006) was implemented (with a scaling factor to achieve improved global mean SW fluxes; see Sect. 3.2). Li et al. (2006) refer to this parametrization as being based on the Preisendorfer and Mobley (1986) scheme. The SZA-dependent land surface albedo is parametrized depending on the surface properties as in Appendix B of Briegleb (1992; analogous to the implementation in the ICON module mo_albedo.f90). For the snow albedo, we use the parametrization as given in Formula A3 of Yang et al. (2001; see also Appendix B of Briegleb, 1992, and references therein).

When the SZA dependence is used, the procedure to calculate the blue-sky albedos is as follows: The white-sky albedo, e.g. from MODIS (see above), is modified according to meteorological properties and land properties as well as ice cover (as was the ECHAM5 background albedo before) and an albedo for sea ice is calculated (again as in ECHAM5). Based on this white-sky albedo and the respective parametrizations (see previous paragraph) a SZA dependent black-sky albedo for land (snow-covered and snow-free) and ice-covered (snow-covered and snow-free) surfaces is calculated. Additionally, over (ice-free) ocean surfaces a white-sky and black-sky albedo is calculated based on the wind speed and the SZA (Yang et al., 2001). From these white-sky and black-sky albedos and the diffuse and direct SW surface radiation fluxes the blue-sky albedo is obtained.

To be able to use this new feature, either the radiation scheme has to provide ~~the (~~(the fraction of) the direct and diffuse SW radiation fluxes from the previous model time step (for the first model time step the partitioning is automatically set to 0.9 and 0.1, respectively) or the user has to set a fixed relation between these fluxes via a namelist. The former is the case for both PSrad and the SW scheme rad_short_v2, which was slightly adapted to this end, whereas the latter is the case for rad_short_v1.

2.6 Minor modifications of the radiation infrastructure

During the restructuring of the radiation infrastructure we made several minor adjustments in addition:

(1): ECHAM5 commonly performs (full) radiation calls less frequently than at each model time step (Roeckner et al., 2003). Thus output from a specific radiation call is used for several model time steps. Hence, at a time step when a new (full) radiation call is performed, the orbital parameters are advanced (by Δt_{orb}) for the radiation call (Roeckner et al., 2003). The results from this radiation call (with the adjusted orbital parameters) are later on ~~adjusted with the~~ corrected with the solar irradiation associated with the orbital parameters of the actual model time step for the calculation of the actual SW fluxes and heating

rates (see Roeckner et al., 2003). We note that the adjusted SZA contains a modification which ensures that fluxes are non-zero globally to avoid problems in the grid boxes in which the sun rises or sets during the time steps associated with the radiation time step (see Roeckner et al., 2003, ; also their Eq. 11.23). Figure 2 illustrates the alignment of model time steps and radiation calls. Previously, the orbital parameters were shifted to the middle of the interval between the current and the next full radiation call, including the latter (Fig. 2a). Now, the offset type can be selected via a new namelist switch. Apart from the previous choice $\Delta t_{orb,opt0}$, which we kept to ensure backward compatibility, the orbital parameters now can be chosen to be calculated for the middle of the interval of time steps associated with the current radiation call ($t_{r,i-1}$, $t_{r,i-1} + \Delta t_m$,..., $t_{r,i} - \Delta t_m$, leading to $\Delta t_{orb,opt1} = \frac{1}{2}((t_{r,i} - \Delta t_m) - t_{r,i-1})$, Fig. 2b), or the offset can be set to an arbitrary constant ($\Delta t_{orb,con} \leq \Delta t_r$). The latter option was introduced for offline radiation calculations.

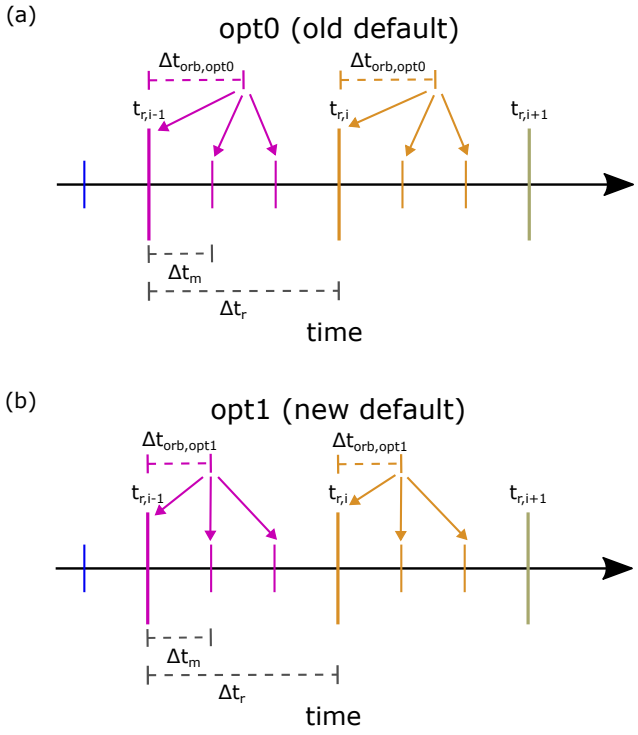

Figure 2. Schematic of the radiation calls for 3 model time steps per full radiation call (long vertical lines, e.g. $t_{r,i}$) for the old (a) and new (b) choice of the offset parameter (Δt_{orb}): For $\Delta t_m < \Delta t_r$ (no full radiation calculation at every model time step), previously (a) the orbital parameters ~~where~~ were shifted according to $\Delta t_{orb,opt0} = \frac{1}{2}(t_{r,i} - t_{r,i-1})$, whereas the new option shifts the parameter according to $\Delta t_{orb,opt1} = \frac{1}{2}((t_{r,i} - \Delta t_m) - t_{r,i-1})$. In addition to the old and new choice of the offset parameter (Δt_{orb}), it is now also possible to set this parameter via a namelist to a constant ($\Delta t_{orb,con} \leq \Delta t_r$).

~~(2): The calculation of the dry air column and the corresponding water vapour, which are passed to the core radiation scheme, were slightly adjusted. In short test simulations we found the effect of the changes to be only of minor importance. As this~~

change had been implemented before the radiation infrastructure was updated, it also applies to the simulations with E5rad. However, for the sake of completeness, we mention it here.

(3): The so-called diffusivity factor (see e.g. Roeckner et al., 2003; Li, 2000, and references in the latter), which is used to scale the optical thickness of the clouds in the LW, was removed from the CLOUDOPT submodel and is now accounted for (exactly once) in the radiation schemes to avoid any confusion. Originally, the application of the diffusivity factor was partly mixed into the parameters that were used to calculate LW cloud optical thicknesses and partly applied later in the code for the new radiation scheme, while it was accounted for in the cloud optical properties for the old scheme. This restructuring caused changes in the output of CLOUDOPT and the binary divergence of model results based on the old and the new code when applying the old (ECHAM5) radiation scheme.

(4): The distance between Sun and Earth (zdisse) was updated to account for the shift of the orbital parameters by Δt_{orb}. Although this change is expected to have a negligible impact on the model results, we note it here, as it destroys binary identity.

2.7 Overview of the new radiation infrastructure dependencies

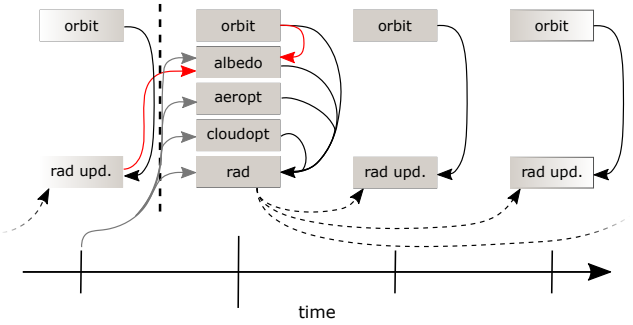

Figure 3. Schematic of the interdependencies of the radiation infrastructure for a typical simulation setup with the new radiation scheme. Grey arrows show information (e.g. temperature, pressure) from the model time step (vertical bars) before a full radiation time step (long vertical bar) that is passed into radiation-related submodels. In a full radiation step (long vertical bar), the radiative transfer is calculated and stored. Dashed arrows: information from a full radiation time step is forwarded to radiation update (rad upd.) time steps. At these time steps for the SW, updates of the radiative fluxes and heating rates are calculated and applied (see Roeckner et al., 2003). Red arrows show new dependencies: Input from the previous radiation update (fluxes at surface) and the information from ORBIT (mainly SZA) are fed to the ALBEDO submodel.

The interplay of the radiation-related submodels is presented as a schematic in Fig. 3 for a typical (new) setup. Red arrows mark the two new dependencies that now exist: 1) The direct and diffuse surface fluxes from the last radiation update (box "rad upd." in Fig. 3) are provided to the ALBEDO submodel. 2) The orbital parameters (most importantly the SZA) are calculated by ORBIT and provided to the ALBEDO submodel, which then calculates the albedo for the next full radiation calculation. We note that the latter dependency was hidden before as the calculation of the surface albedo was performed in the RAD submodel. While the other dependencies (black arrows) have already existed before our developments, all submodels (RAD, ALBEDO,

CLOUDOPT, AEROPT) except for ORBIT have been revised and are more flexible now.

The processing chain of the radiation calculation is as follows: At a full radiation time step (long vertical bar in Fig. 3), the information (e.g. temperature, pressure, cloud, aerosol, gases, ...) from the previous model time step is available to ALBEDO, AEROPT, CLOUDOPT and RAD. Additionally, fluxes from the last radiation update are available for the ALBEDO submodel, which also receives information from ORBIT, in particular the SZA. Then, the different radiation related submodels are called and pass their information to RAD. Finally, the full radiation calculation is performed with an offset of the orbital parameters and the results are stored. The SW fluxes at the model time steps are then calculated via a simple update of the radiation fluxes (as in ECHAM5 see Roeckner et al., 2003). Note that "rad upd." is also performed for the full radiation time step as the orbital parameters used for the radiative transfer are typically shifted in comparison to the orbital parameters (mainly SZA) associated with the current model time step (see Δt_{orb} Sect. 2.6).

3 Evaluation of the new (~~dynamic~~GCM-type) configuration

During the implementation of the presented updates, it was ensured that previous model results could be reproduced after the restructuring of the code. In particular, binary identity was secured up to a point, where required changes (see Sect. 2.6, e.g. "diffusivity factor") break binary identity. A key strength of the MESSy concept is that many (including previous) model configurations can be run with the same executable by adjusting Fortran namelists only. Accordingly, the four simulations discussed hereafter can be performed with the same executable by changing three namelist files (RAD, ALBEDO and IMPORT) only. As we have performed diagnostic radiation calls with an exchanged radiation scheme (e.g. driving the simulation with PSrad and performing an additional diagnostic radiation call with E5rad; see Sect. 4), the CLOUDOPT and AEROPT namelist files already included the calculation of aerosol and cloud optical properties for both (E5rad and PSrad) radiation schemes. Hence, these namelist files did not have to be adjusted when the driving radiation scheme was switched.

3.1 Simulation setups

We performed four simulations for the evaluation presented here. Namely, two simulations (pre-industrial and present-day denoted with pi and pd, respectively) for each of the two radiation schemes (the old ECHAM5 radiation scheme with the v2 in the SW, denoted here with E5rad, and the newly implemented PSrad scheme). These simulations will be addressed here as EMAC-E5rad-pi, EMAC-E5rad-pd, EMAC-PSrad-pi and EMAC-PSrad-pd, respectively. The simulation setups do not differ only in the radiation scheme but also according to the respective radiation scheme the typical old and new setups of AEROPT, CLOUDOPT and ALBEDO (as described before) have been chosen as indicated in Table 1. In all simulations the new choice for the orbital offset parameter (Δt_{orb}) was employed.

The simulations were conducted with T42 spectral truncation (corresponding to about 2.8° × 2.8°, i.e. roughly 300 km × 300 km at the equator) and 90 vertical levels extending up to roughly 80 km (see the T42L90MA setup e.g. mentioned by Jöckel et al., 2016). The model time step length was set to 600 s and full radiation calculations were performed every third model time step.

For the solar forcing we applied a total solar irradiance (TSI) of 1360.75 $\mathrm{Wm^{-2}}$, representing approximately the average TSI of the first two decades (first two solar cycles) in the time series displayed in Fig. 1 of Matthes et al. (2017a; Matthes et al., 2017b; data also available from https://solarisheppa.geomar.de/cmip6), i.e. representing pre-industrial conditions. Although Fig. 1 of Matthes et al. (2017a) indicates an increase in TSI from the pre-industrial conditions to the end of the 20th century (to roughly 1361.25 $\mathrm{Wm^{-2}}$), we have kept the TSI constant for the present-day simulations. The increase of about 0.5 $\mathrm{Wm^{-2}}$, is not of substantial relevance in the global energy budget of Earth, as only 1/4 of this difference remains for Earth's global average, which is further reduced as a part of this additional solar irradiance is reflected. Thus we expect the change from pre-industrial to present-day conditions to be in the order of about 0.1 $\mathrm{W\,m^{-2}}$ in the end.

Table 1 presents additional forcings and boundary conditions. These represent pre-industrial (pi, representative of the year 1850 conditions with some deviations due to data availability) and present-day conditions (pd, representative of the year 2000 conditions). A short outline of the employed boundary data is given below.

The four simulations use prescribed sea surface temperatures (SSTs) and sea ice cover (SIC; Rayner et al., 2003) and the quasi-biennial oscillation (QBO) is nudged as described by Jöckel et al. (2016). Except for simplified methane chemistry, these simulations ~~are purely dynamic~~feature no chemistry and are thus described here as GCM-type simulations as opposed to chemistry-climate model simulations. In the lowest model level methane (CH_4) is nudged to surface mixing ratios according to historical CMIP6 data (Meinshausen et al., 2017). In the atmosphere the simplified methane chemistry includes two effects: (i) The methane oxidation, which is represented by the MESSy submodel CH4 (Winterstein and Jöckel, 2021) using prescribed climatologies of the methane reactions partners (OH, $O(^1D)$, Cl) from previous EMAC simulations: EMAC-DECK-piControl and EMAC-RD1-base-01 (Jöckel, 2023, see also https://data.ceda.ac.uk/badc/ccmi/data/post-cmip6/ccmi-2022/DLR/EMAC-CCMI2/refD1),which were conducted according to the CMIP6 (Eyring et al., 2016) and CCMI-2 (https://blogs.reading.ac.uk/ccmi/ccmi-phase-two/, accessed last 17 July 2023; for phase one of CCMI see Eyring et al., 2013; Morgenstern et al., 2017) protocols. Water vapour tendencies due to methane oxidation are consequently accounted for in the interactive water vapour field of the simulation. (ii) Methane is photolyzed using a photolysis rate which is calculated online by the MESSy submodel JVAL (Sander et al., 2014). The corresponding water vapour and methane fields are used in the first call of the radiation module and thus are driving the simulation.

All other trace gas fields required by the radiation schemes, e.g. carbon dioxide (CO_2), nitrous oxide (N_2O), ozone (O_3) and the chlorofluorocarbons CFC-11 and CFC-12, also stem from comprehensive chemistry-climate model simulations, which were previously conducted with EMAC, namely EMAC-DECK-piControl and EMAC-RD1-base-01. Additional diagnostic radiation calls were performed with the imported methane fields from these previous EMAC simulations.

The CO_2, CH_4 and N_2O fields of these previous simulations in turn are based on the respective historical CMIP6 data presented by Meinshausen et al. (2017), which are used as lower boundary conditions in these simulations. Table **??** presents the climatological surface level mixing ratios of these simulations. These values are in agreement with the values presented in Table 5 of Meinshausen et al. (2017) for 1850 and 2000 conditions.

For CFC-12 the global mean values in the lowest model level are 0 and 528.7 pmol mol^{-1} for pi and pd conditions, respectively (see Tab. **??**). These values are in agreement with the lower boundary values they are based on, which were presented by Meinshausen et al. (2017) and Carpenter et al. (2018). To include the effect of additional radiatively active ozone-depleting substances (ODSs), the approach outlined by Meinshausen et al. (2017) to lump additional radiatively active ODSs via radiative efficiencies (see e.g. Burkholder, 2018) to CFC-11 equivalents for purposes of radiative transfer calculations was applied in the EMAC-DECK-piControl and the EMAC-RD1-base-01 simulations. For the EMAC-DECK-piControl, eight species have

been lumped to CFC-11 equivalents based on values presented by Meinshausen et al. (2017), whereas for the EMAC-RD1-base-01 only six species have been lumped according to the data given by Carpenter et al. (2018). This results in global mean values of 2.4 pmol mol^{-1} and 492.8 pmol mol^{-1} of CFC-11 equivalents in the lowest level of the EMAC-DECK-piControl and EMAC-RD1-base-01 simulation, respectively. This is lower than the expected full CFC-11 equivalents for the respective periods, which are in the order of 30 pmol mol^{-1} for pre-industrial conditions and above 700 pmol mol^{-1} for the 2000s (see Meinshausen et al., 2017). However, the lower CFC-11 equivalent mixing ratios in the EMAC simulations, are in agreement with the respective reference values given the reduced number of accounted (lumped) species in the model setups.

In all simulations stratospheric aerosol data from the ETH Zürich (ETHZ) (2017), as proposed for CMIP6, were employed. The tropospheric aerosol data is based on Tanre et al. (1984) and Kinne et al. (2013) for E5rad (as described by Roeckner et al., 2003, for ECHAM5) and PSrad, respectively. Concerning the surface albedo, the E5rad simulations use the previous ECHAM5 routines to adapt the ECHAM5 background albedo (for details see Hagemann, 2002; Roeckner et al., 2003), whereas the PSrad simulations use the surface albedo computed with the newly implemented solar zenith angle dependent albedo (for water, land and snow), where the white-sky albedo for snow-free land was derived from MODIS (see Sect. 2.5). Hence, except for tropospheric aerosol data and the albedo, the boundary conditions for the E5rad and PSrad simulations were identical.

After optimizing the set of free parameters of the model with respect to the boundary data and the respective radiation scheme (see description in Sect. 3.2), the simulations have been performed for 20 years, while our analyses exploit only the last 10 years of each of the simulations to reduce the risk of any possible influence from the spin-up period. To reduce the amount of data, model output was aggregated as monthly mean values on model levels. These monthly means were calculated online (i.e. all model time steps are accounted for in the means) and, whenever necessary, they were interpolated to pressure levels offline.

Without additional diagnostic radiation calls for RF calculations as presented in Section 4, for a simulation performed on a single node[1] the computational time required for a radiation time step is around 70% higher for the PSrad setups than for the E5rad setups. If the full radiation calls are only performed every third time step (as in the simulation setups described above), this leads to an increase in the computational time of roughly 40%. This increase in computational time cannot be solely attributed to the core radiative transfer routines in RAD but is also affected by possible changes in computational time in the connected submodels AEROPT, CLOUDOPT and ALBEDO. To put this increase into perspective, we note that EMAC is commonly used in setups with comprehensive interactive chemistry (e.g. as chemistry-climate model). Due to the large computational demand of the chemistry solver the increase in computational time due to the radiation scheme will only be a fraction of the increase we report here for a GCM-type setup.

[1] 32 task on an AMD Epyc 7601 node with 32 cores

3.2 Parameter optimization for the ~~dynamic model~~ GCM-type setups

Earth receives approximately 0.34 kW m^{-2} of solar radiation at the top of the atmosphere (TOA) on average, which is almost balanced by TOA reflected SW radiation ($\sim$ 0.1 kW m^{-2}) and TOA outgoing LW radiation ($\sim$ 0.24 kW m^{-2}; e.g. Trenberth et al., 2009; Stephens et al., 2012; Wild et al., 2015). It is challenging to assess the resulting imbalance (Johnson et al., 2016), which is somewhat below 1 W m^{-2} (e.g. Trenberth et al., 2009; Wild et al., 2015; Johnson et al., 2016, which present estimates within 0.6–0.9 W/m^2). The best estimates are derived from heat uptake analyses (Johnson et al., 2016), which are used to calibrate satellite-based observations (Loeb et al., 2009, 2018).

Similarly, in global (climate) models the TOA (im)balance is commonly "calibrated" to observed estimates during the so-called tuning process (Hourdin et al., 2017). Here, we optimize the four setups that are described in the section above (Sect. 3.1). Our two primary targets were (i) a radiative balance at TOA close to 0 Wm^{-2} for the pre-industrial configuration (assuming that during that period the Earth's energy budget was almost balanced) and (ii) a radiative imbalance at TOA around 1 Wm^{-2} for the present-day configuration with the same parameter set (accounting for the expected imbalance; see above). Further, we aimed for clear- and all-sky LW and SW present-day TOA radiation fluxes to be within the uncertainty range of satellite-based observational estimates (Loeb et al., 2018; CERES Science Team, 2021), while securing the hydrological cycle to remain within an acceptable range compared to observations (see below). For a more elaborate review of the principles of climate model tuning, which we will address also as parameter optimization in the following, we refer the reader to Mauritsen et al. (2012).

To achieve our goals, we adjusted parameters associated with clouds, convection and the surface albedo, while keeping the previous defaults e.g. for parameters related to the parametrization of gravity waves. Table 2 lists the final parameter set along with previously used parameter values. Prior knowledge of sensitivities of the radiative fluxes regarding typical optimization parameters from Mauritsen et al. (2012; Fig 3) and Kern (2013; Appendix D) allowed us to adjust parameters in a target-oriented manner without extensive testing of all possible sensitivities.

As a starting point for the model optimization, we used typical ECHAM6.3 values for the inhomogeneity factors for liquid and ice clouds (Mauritsen et al., 2019). All other optimization parameters were set to the previous EMAC defaults. Firstly, we targeted the TOA global annual mean clear-sky SW fluxes via the surface albedo as there is no (substantial) dependence of these fluxes on the other optimization parameters. During this process, we increased the minimum albedo of bare sea ice from 0.50 (see Roeckner et al., 2003) to 0.55 (a value that has been previously used in other EMAC simulation setups) and increased the ocean surface albedo by a factor of 1.15 to enhance the outgoing SW clear-sky radiation at TOA to roughly match satellite-based estimates (Loeb et al., 2018). Secondly, we targeted the TOA LW flux by increasing a parameter that influences a geopotential-based conversion rate from cloud water to rain in convective clouds (cprcon) to the value used for ECHAM6.3 in T63 spectral resolution (Müller et al., 2018). Thirdly, targeting the TOA SW flux, which is sensitive towards various parameters

(see e.g. Mauritsen et al., 2012), we decreased the convective mass flux above the level of non-buoyancy (cmfctop) to 0.23, which now lies between the previous EMAC default and the value used in ECHAM6.3 in T63 spectral resolution (Müller et al., 2018).

Figure 4 shows various radiation fluxes along with reference values from observations (Loeb et al., 2018; CERES Science Team, 2021) and results from CMIP6 (Wild, 2017). Both, the observations and the CMIP6 results in Wild (2017) are representative of present-day conditions. The global mean radiation (im)balance in the EMAC simulations is somewhat above 1 W m^{-2} for present-day conditions and somewhat below 0 W m^{-2} for pre-industrial conditions with slightly more deviation from the target values for the E5rad simulations. The absolute values of the LW and SW all-sky fluxes are slightly too low on average in the EMAC simulations compared to observational data. Overall the various fluxes from the optimized simulations lie close to or within the uncertainty range of observations.

3.3 Comparison of old and new model configuration

After optimizing the model configurations for pre-industrial and present-day conditions, we compare the climatological mean states of key meteorological quantities with reanalysis and observational data. For the reanalysis data we employ ERA5 (Hersbach et al., 2020) monthly mean data on pressure levels (Hersbach et al., 2023) obtained from Copernicus Climate Change Service, Climate Data Store (2023). The model data was interpolated vertically to the pressure levels of the reanalysis (pressure level) data set, whereas the ERA5 data was horizontally regridded to the T42 resolution of the model data. For the evaluation of simulated precipitation data, we use the monthly mean observational data from the Global Precipitation Climatology Project (GPCP, e.g. Huffman et al., 1997, 2009; Adler et al., 2003) version 2.3 (Adler et al., 2018). For both reanalysis and observational data we use the period 2000–2009 for intercomparison with the last ten years of our simulations (see Sect. 3.1).

Figure 5 shows the differences in the zonal mean temperatures between the model present-day configurations and ERA5 (first two columns) and between the two present-day simulations with different driving radiation schemes (PSrad and E5rad, third column). Up to around 30 hPa, both model configurations show similar bias patterns compared to ERA5. These biases tend to be lower for EMAC-PSrad-pd than for EMAC-E5rad-pd, except for the extratropical stratosphere in the height region between 150 and 30 hPa. Above 30 hPa EMAC-PSrad-pd shows mostly higher temperatures than EMAC-E5rad-pd. Hence, where E5rad was on average too cold in the region above 30 hPa the EMAC-PSrad-pd simulation results seem to be too warm in comparison with ERA5 data and the warm bias at 60-40° S during ~~JJA~~ June-July-August (JJA) compared to ERA5 is even more pronounced in EMAC-PSrad-pd. However, in large regions EMAC-PSrad-pd performs better e.g. concerning the cold bias around the tropical cold point (which is reduced by about 3 K) and the reduced cold bias in the extratropical lower stratosphere.

The cold bias in the tropical upper troposphere and lower stratosphere, as well as other biases of EMAC-E5rad-pd compared to ERA5 are similar to what has been found by Jöckel et al. (2016) when comparing annual climatologies of EMAC

simulations with ERA-Interim data (see their Fig. 12; in particular the panel for the RC1-base-01 simulation). Previous comparisons of ECHAM5 and ERA-Interim data for ~~DJF~~ December-January-February (DJF) presented by Stevens et al. (2013) show similar biases as our EMAC-E5rad-pd simulation (see their Fig. 12). Stevens et al. (2013) also find a resolution-dependent warming and a reduction of the cold biases during DJF when ECHAM6.1 (including an updated radiation scheme compared to ECHAM5) is employed. These changes from ECHAM5 to ECHAM6.1 are similar to the improvements we have found when assessing EMAC-PSrad-pd compared to EMAC-E5rad-pd simulations.

Figure 6 shows the corresponding zonal mean zonal wind differences. The main biases between the model data and ERA5 remain unchanged when the newly available radiation scheme, PSrad, is used. These biases have already been present in comparisons of ERA-Interim data with ECHAM5 and ECHAM6.1 data (Stevens et al., 2013, see their Fig. 13). EMAC-PSrad-pd shows reduced biases at 60° S in comparison to EMAC-E5rad-pd. However, in the SH polar region during JJA above 50 hPa the positive bias is increased in EMAC-PSrad-pd. In the tropical upper troposphere eastward winds are present in EMAC-E5rad-pd, whereas ERA5 shows westward winds in this region. This bias slightly increases in the simulation with PSrad. Differences between EMAC-E5rad-pd and EMAC-PSrad-pd show increased wind speeds during JJA in the SH polar vortex (Fig. 6i). This strengthening of the polar vortex is desirable as the polar vortex in EMAC is known to be too weak (Jöckel et al., 2016).

Although the analyses only include the last 10 years of both the E5rad-pd and the PSrad-pd simulation, the results from the pre-industrial simulations support the general features presented here. In particular, the patterns of the differences that arise when employing the new radiation scheme (PSrad) and the previous ECHAM5 scheme (E5rad) are similar under present-day and pre-industrial conditions.

Figure 7 shows specific humidity profiles (in kg per kg of moist air) for different latitudinal bands from the tropics to the high latitudes. Overall, all data sets show the typical decrease of specific humidity with height in the troposphere. Above approximately 100 hPa, ERA5 shows higher specific humidity than the model data. At this altitude, the EMAC-PSrad-pd simulation is moister (and thus in better agreement with ERA5) than the EMAC-E5rad-pd simulation, which is consistent with higher tropical cold point temperatures in the EMAC-PSrad-pd simulation compared to the EMAC-E5rad-pd simulation (see Fig. 5). In general, ERA5 reaches the low stratospheric humidity values somewhat below (at higher pressures than) the model data. This is particularly obvious in the NH and SH polar cap profiles, where in the height region near 200 hPa ERA5 has already reached minimum specific humidity values in the range of 2-3$\times 10^{-6}$ kg kg^{-1} and the EMAC simulations still show a roughly linear decrease in specific humidity (in log-log) up to somewhat below 100 hPa. Due to a slower decrease and a slight kink in the specific humidity profiles over the polar cap regions in the EMAC simulations, specific humidity values are higher in the EMAC simulations than in ERA5 around 200 hPa over the polar caps. After reaching the minimum specific humidity values in the upper troposphere–lower stratosphere region, the specific humidity values increase slightly with height. We attribute this increase to the moistening through methane oxidation, which increases with height up to at least 10 hPa in the model (Eichinger

and Jöckel, 2014, see their Fig. 8).

Seasonal variations of tropical stratospheric water vapour related to the water vapour tape recorder (Mote et al., 1996) are shown in Fig. 8 for the last 10 years of the EMAC simulations and the period from 2000 to 2009 for ERA5. An intercomparison is feasible due to the selection of the transient SSTs and the nudging of the QBO in the EMAC simulations (see Table 1). The left panels (Fig. 8a and c) show the time series of specific humidity at 70 hPa and 50 hPa averaged over 10° S–10° N. All data sets show a clear seasonal variation and, as noted before, EMAC-PSrad-pd shows higher values than EMAC-E5rad-pd, which are in better agreement with ERA5. The amplitudes of the seasonal cycle of stratospheric water vapour are largest in ERA5 and smallest in the EMAC-E5rad-pd simulation. According to Brinkop et al. (2016), this can be attributed to the too low tropical cold point temperatures in EMAC-E5rad-pd. From comparing panels a) and c) of Fig. 8 the time lag of the water vapour signal propagation is apparent. Further, the amplitudes of the water vapour variations decrease with height in all data sets as can be expected (Mote et al., 1996, 1998).

To assess the amplitude of the variations, Fig. 8 also shows the relative anomalies of specific humidity for the same region (panels b and d). We calculated the relative anomalies as $(q(t) - \overline{q})/\overline{q}$, where $q(t)$ is the monthly specific humidity value and the overbar denotes the mean (all months weighted equally) of the displayed period. The amplitude and signal strength are captured better in EMAC-PSrad-pd than in EMAC-E5rad-pd when taking ERA5 as a reference. Similar to the absolute amplitudes, the relative amplitudes also decrease with height.

Due to a setup inconsistency ERA5 has a cold bias in the stratosphere for the period 2000 to 2006, which also affects stratospheric water vapour (Simmons et al., 2020). This issue has been addressed in a new set of analyses called ERA5.1 covering this period (Simmons et al., 2020). We note however, that the differences between ERA5.1 and ERA5 regarding temperatures and water vapour as analysed by Simmons et al. (2020) are relatively small compared to the differences we see between ERA5 and our model simulations. Hence we simply applied the ERA5 data as the main conclusions regarding the model reanalyses differences will remain unchanged.

Figure 9 shows the 10-year mean zonal mean precipitation for the model data and GPCP v2.3. Table 3 presents the corresponding tropical (30° S–30° N) and global means. Overall, the largest differences between model and observational data are found in the tropics (30° S–30° N) and in the region 40° S–70° S. In the tropics all simulations show enhanced precipitation in comparison to the observational data. On average, the tropical (30° S–30° N) mean precipitation lies between 3.62 and 3.78 mm day^{-1} in the simulations, whereas GPCP v2.3 shows 3.05 mm day^{-1}. Further, the different simulation periods of pi and pd seem to have a smaller impact on the precipitation distribution than the exchange of the radiation scheme, i.e. blueish (reddish) lines are more similar than solid (dashed) lines, respectively. The global mean precipitation is 3.00–3.11 mm day^{-1} in the simulations and 2.70 mm day^{-1} in the GPCP v2.3 data. Both, the distribution of simulated precipitation and the global

575 and tropical mean values are comparable to previous EMAC results presented by Jöckel et al. (2016, their Fig. 13), where only EMAC simulations which include global mean temperature nudging showed considerably less precipitation.

Table 1 (previous Table 2 of the discussion version) has been restructured and adapted for the revised version.

Table 1. Boundary conditions of the simulations for pre-industrial and present-day conditions with radiation scheme E5rad and PSrad. Monthly mean data is abbreviated via mm. Please see the text for details.

Data/Forcing	Source (reference)	type	
		pre-industrial: pi	present day: pd
SST/SIC	HadISST (Rayner et al., 2003)	mm transient (1875-1894)	mm transient (1990-2009)
QBO	FUB (Naujokat, 1986)*	mm transient (1875-1894)	mm transient (1990-2009)
O_3, OH, Cl, $O(^1D)$, CH_4, CO_2, N_2O, CFC-11 eq., CFC-12	EMAC-DECK-piControl (CMIP6)	mm climatology from 20 years of 1850 time slice	
	EMAC-RD1-base-01 (CCMI-2)		mm climatology from transient run 1990-2009
CH_4 (call 01)**	Meinshausen and Vogel (2016); Meinshausen et al. (2017) (CMIP6)	mm of year 1850 (cyclic) as lower boundary and CH4 sub-model	mm of year 2000 (cyclic) as lower boundary and CH4 sub-model
strat. aerosol	ETH Zürich (ETHZ) (2017) (CMIP6)	mm of year 1850 (cyclic)	mm of year 2000 (cyclic)
	EMAC-E5rad setups		
trop. aerosol	Tanre et al. (1984)	climatology	
albedo	Hagemann (2002)	background albedo modified according to meteorological and land properties (as in ECHAM5, Roeckner et al., 2003, see text for details)	
cloud optical properties	ECHAM5 (Roeckner et al., 2003)	see text for details	
	EMAC-PSrad setups		
trop. aerosol	Kinne et al. (2013)	mm of year 1865 (cyclic)***	mm of year 2000 (cyclic)***
albedo	MODIS (Sun et al., 2017; Schaaf, 2019)	mm climatological white-sky albedo based on MODIS modified according to meteorological and land properties (as in ECHAM5, Roeckner et al., 2003) and parametrizations for SZA dependence (see text for details)	
cloud optical properties	ECHAM6 (Stevens et al., 2013)	see text for details	

*): For the QBO an extension method (see https://www.pa.op.dlr.de/CCMVal/Forcings/qbo_data_ccmval/u_profile_195301-200412.html for a description, last access 19 July 2023) was applied to observational data available from FUB (https://www.geo.fu-berlin.de/en/met/ag/strat/produkte/qbo/index.html, last access last access 19 July 2023; see also Naujokat, 1986).

**) Lower boundary conditions and simplified methane chemistry were used to produce the CH_4 field, which drives the simulations. However, for additional radiation calls the CH_4 from previous EMAC simulations as for other GHGs, is being used to ensure that the CH_4 fields are identical in the simulation driven with E5rad and PSrad and that they match with the other GHGs.

***) The aerosol data set by Kinne et al. (2013) is a mm climatology for the coarse aerosol whereas the fine mode aerosol is mm transient (see also Giorgetta et al., 2013b).

Table 2. Comparison of optimized parameters for the final simulation setups with previously used values. Note that the parameter values for the newly optimized simulations (middle column) are within an acceptable range of previously used parameter sets for ECHAM (right column).

Parameter	EMAC-PSrad/E5rad values	ECHAM reference values
inhomogeneity factors for liquid clouds (zinhoml)*	0.80 / 0.40 / 0.80	0.80 / 0.40 / 0.80 (Mauritsen et al., 2019)**
inhomogeneity factor for ice clouds (zinhomi)	0.80	0.80 (Mauritsen et al., 2019)
parameter to influence the geopotential-related conversion rate from cloud water to rain in convective clouds (cprcon in $s^2\,m^{-2}$)	2.5×10^{-4}	2.5×10^{-4} (Müller et al., 2018)***
convective mass flux above the level of non-buoyancy (cmfctop)	0.23	0.20 (Müller et al., 2018)***
minimum albedo of bare sea ice (calbmin)	0.55	0.5 (Roeckner et al., 2003)
new scaling parameter for the solar zenith angle dependent ocean surface albedo (osapmfac)****	1.15	-

*) For radiation calls with the old radiation scheme, E5rad, zinhoml is calculated based on total liquid water path an another parameter (zinpar) according to eq. 11.52-11.53 in Roeckner et al. (2003).

**) Mauritsen et al. (2019) only discern certain shallow convective clouds with a different zinhoml factor; this is accounted for by setting two of the three zinhoml parameters to 0.8 in our simulations.

***) Here, we cite the parameters as listed for MPI-ESM1.2-LR by Müller et al. (2018).

****) Only applicable for simulations driven by PSrad

Table 3. Annual mean precipitation ($mm\,day^{-1}$) over the last ten years of the simulations and for 2000–2009 for GPCP_v2.3 data.

	tropics (30° S–30° N)	global
EMAC-E5rad-pi	3.75	3.08
EMAC-PSrad-pi	3.62	3.00
EMAC-E5rad-pd	3.78	3.11
EMAC-PSrad-pd	3.62	3.01
GPCP_v2.3	3.05	2.70

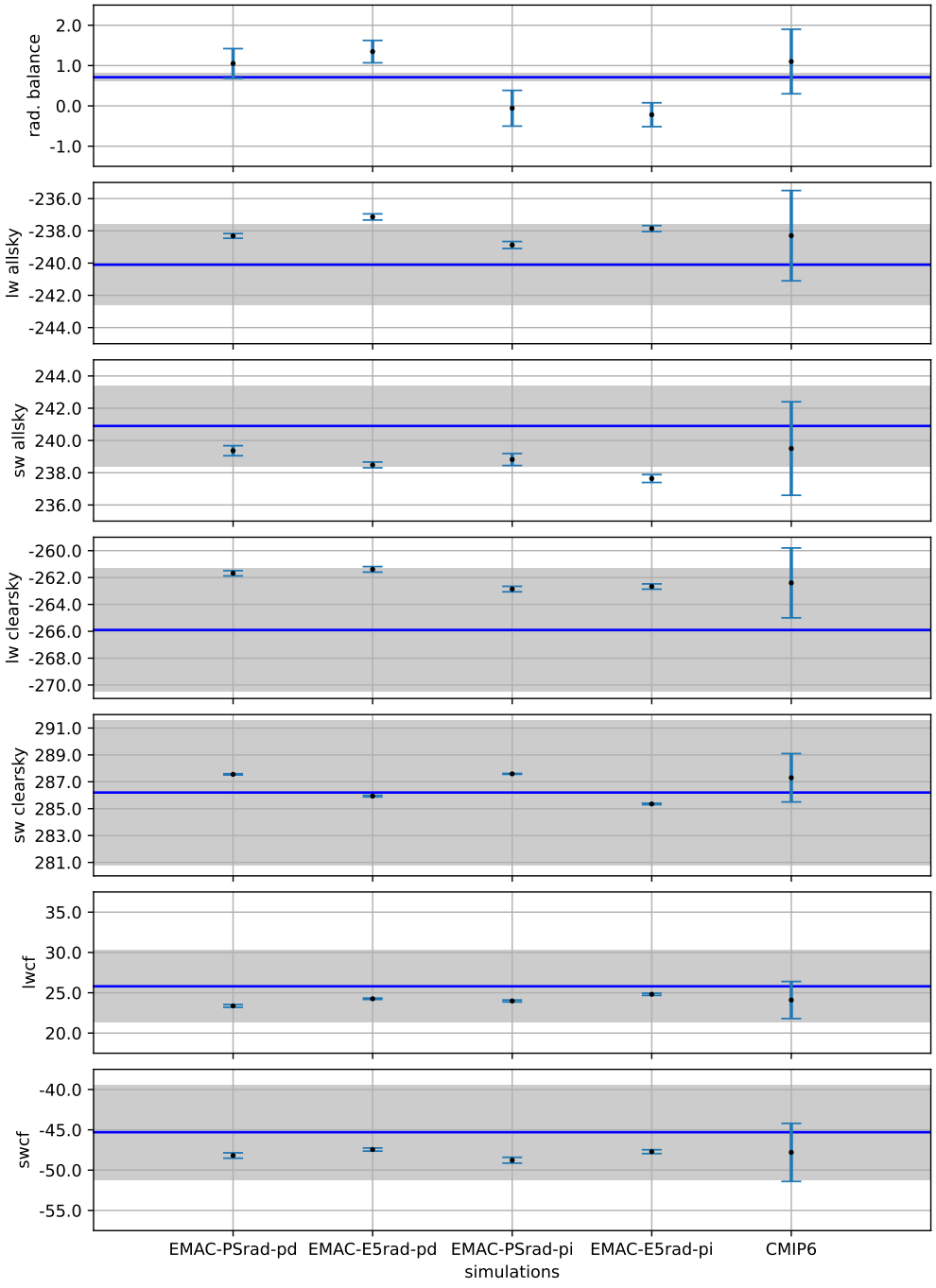

Figure 4. Radiation fluxes (in $\mathrm{W\,m^{-2}}$) for the pi and pd simulations driven by E5rad and PSrad in comparison to estimates from observational data. The estimates (blue horizontal lines) are based on Loeb et al. (2018) with updates presented by the CERES Science Team (2021). The grey shading marks the respective uncertainties and we aimed for the radiation fluxes (mainly from the pd simulation) to be located within the shaded region after completion of the optimization process. CMIP6 data from Wild (2017) shows the multi-model mean and the inter-model standard deviation.

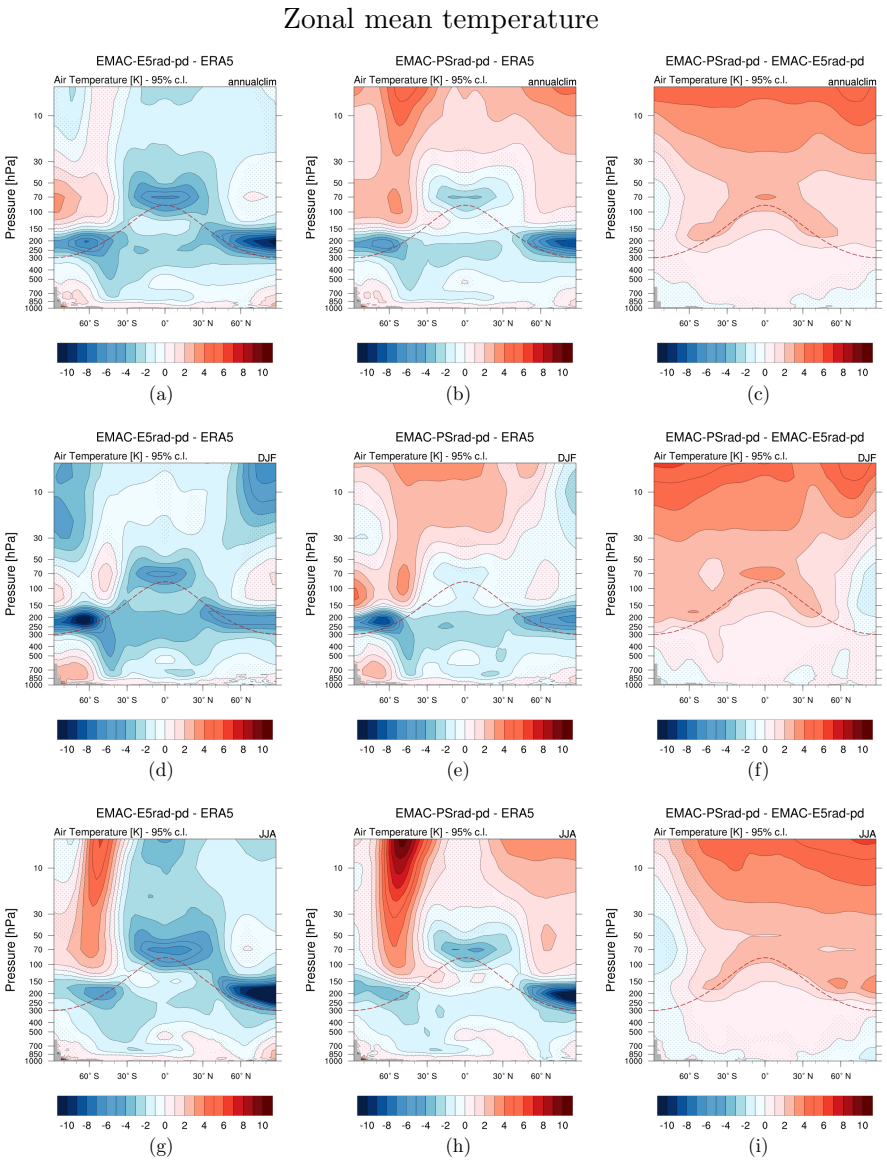

Figure 5. Differences of multiannual zonal mean temperatures between EMAC-E5rad-pd and ERA5 **(a, d, g)**, EMAC-PSrad-pd and ERA5 **(b, e, h)**, and the differences between EMAC-E5rad-pd and EMAC-PSrad-pd **(c, f, i)**. Differences in the annual means are shown in the first row, whereas the second and third row show differences for DJF and JJA means, respectively. Stippled regions are not significant on the 95% level based on Welch's t-test. The dashed line indicates a simple latitudinally-dependent approximation of the tropopause (Jöckel et al., 2000).

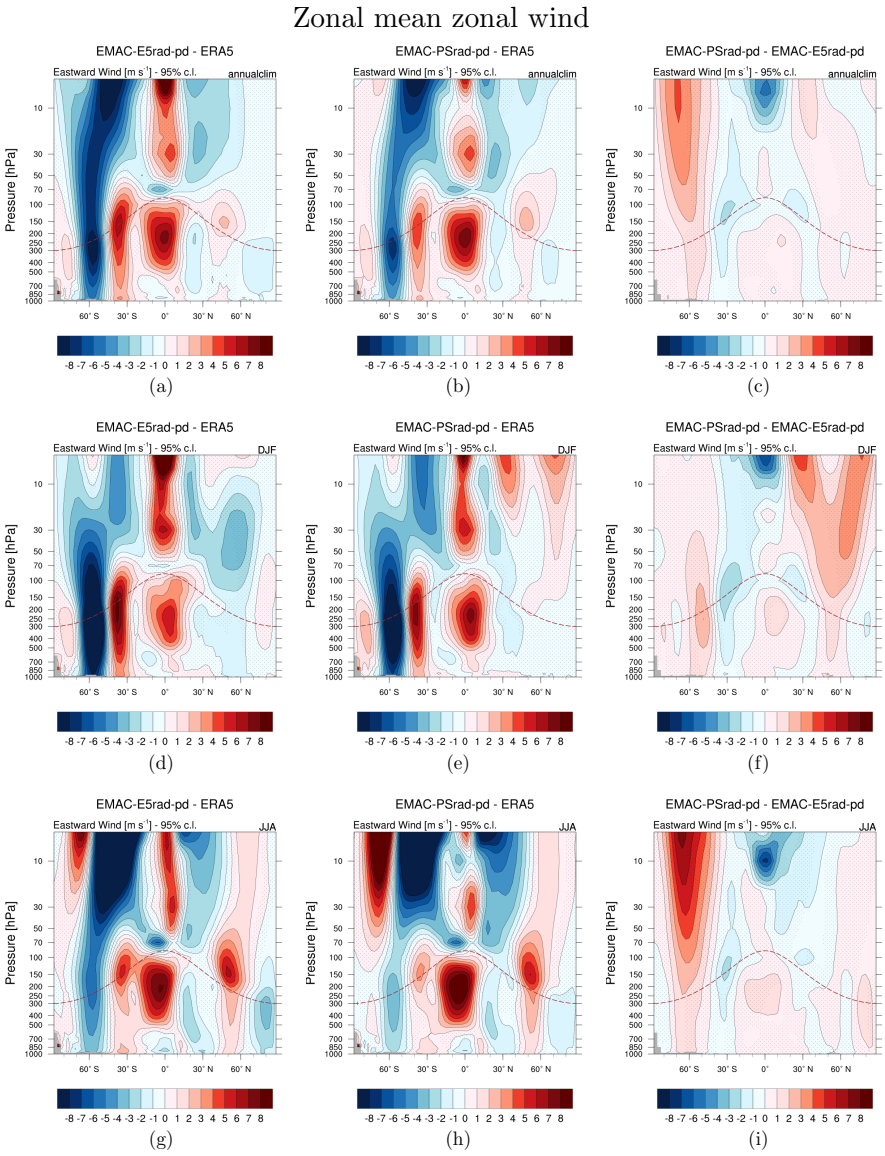

Figure 6. As in Fig. 5 but for the differences of multiannual zonal mean of zonal winds.

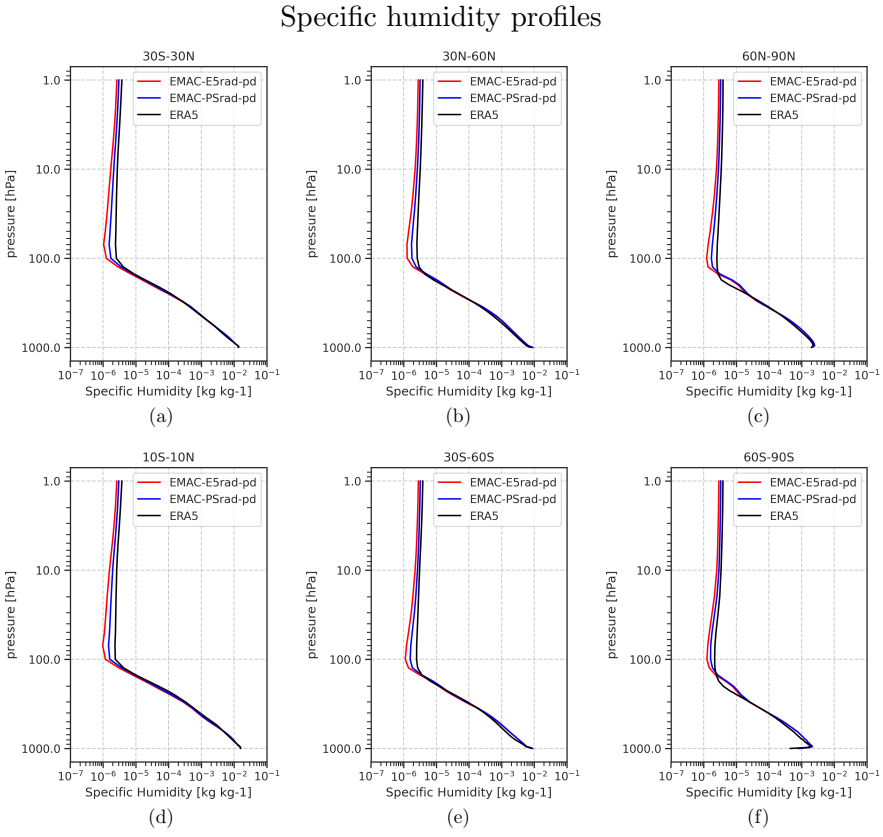

Figure 7. Profiles of specific humidity ($\mathrm{kg\,kg^{-1}}$) for various latitudinal bands based on a 10-year climatology. The bands are for the tropics 30° N–30° S **(a)** and 10° S–10° N **(d)**, the extratropics 30–60° N/S **(b)/(e)** and the polar region 60–90° N/S **(c)/(f)**.

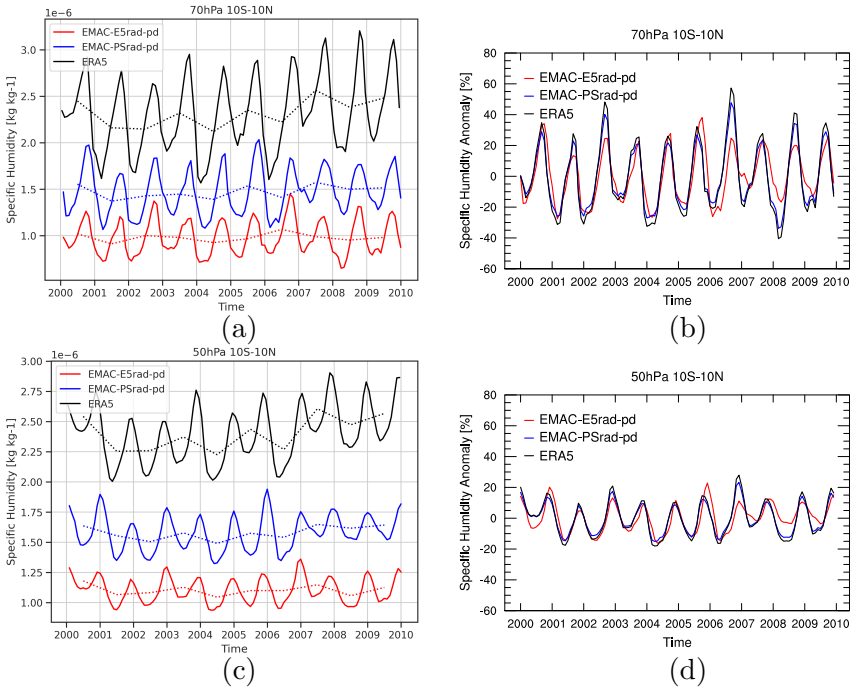

Figure 8. Tape recorder signal at 70 hPa (top row) and 50 hPa (bottom row) given by the specific humidity averaged over 10° S–10° N. **(a, c)** Time series of specific humidity in 10^{-6} kg kg^{-1}. **(b, d)** Relative anomaly (in percent) of the tape recorder signal, i.e. displayed is the relative anomaly with respect to the respective long-term mean (all months weighted equally).

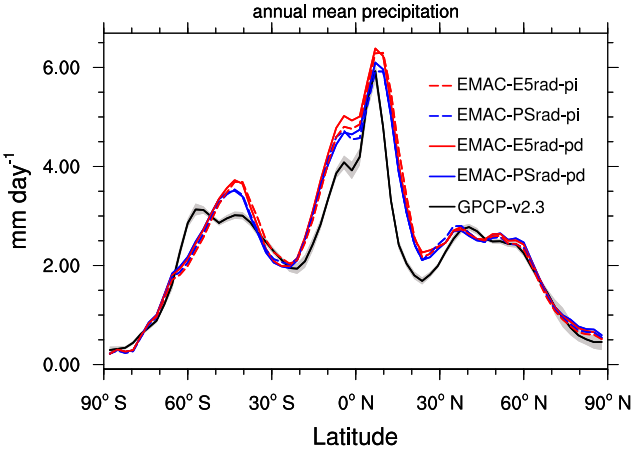

Figure 9. Multiannual zonal mean precipitation (mm day^{-1}) for the last ten years of the simulations and the period 2000–20009 for GPCP v2.3 data. GPCP v2.3 was conservatively regridded to a T42 grid using Climate Data Operators (CDO, https://code.mpimet.mpg.de/projects/cdo/ last accessed 21 August 2023).

4 Radiative forcing calculations using multiple diagnostic calls

We use the simulations of the newly optimized model configurations to assess RFs due to perturbations of GHGs in the old and new model setups.[2] A central objective of the intercomparison presented here is to enable the attribution of differing RF results either to differences in the background meteorology or to differences in the actual radiative transfer calculation, as well as to assess the impact of different GHG backgrounds on the RF values related to a perturbation. To this end, additional diagnostic calls of the radiation scheme with perturbed GHGs (namely, CO_2, N_2O, CH_4 and CFCs) have been conducted in both the simulations under pre-industrial and present-day conditions, which employ once the ECHAM5 radiation scheme (E5rad) and once the PSrad radiation scheme for driving the simulation. The respective GHG fields were adopted from previous EMAC simulations (see Tab. 1), except for the methane field which enters the first call of the radiative transfer calculation and drives the simulation (see Sect. 3.1).

Table 4 lists the respective perturbations that are calculated in the multiple calls of the radiation scheme. In total, 22 additional (diagnostic) calls for calculating instantaneous RF (calls 02 to 23) and 11 additional calls for calculating stratospheric adjusted RF ~~(calls 24 through 34) have been~~ (calls 24 through 34, where stratospheric adjustment is calculated as described by Stuber et al., 2001) , were conducted. In the columns of Table 4 the perturbations are listed, for example for call 03 (call 25), CO_2 has been set to present-day values for the pi simulations and to pre-industrial values for the pd simulations. Thus, the instantaneous (stratospheric adjusted) RF due to increasing CO_2 from pre-industrial to present-day levels can be assessed from $F_{pi;CO_2(pd)} - F_{pi}$ or alternatively from $F_{pd} - F_{pd;CO_2(pi)}$. The first subscript denotes the reference state, the second subscript (if present) denotes the species that has been perturbed and F denotes the instantaneous (stratospheric adjusted) TOA radiative fluxes from call 02 and call 03 (call 24 and call 25), respectively. This may be viewed as the adoption of the forward and backward calculation method (known from radiative feedback analysis, for example, Colman and McAvaney, 1997; Klocke et al., 2013; Rieger et al., 2017) for the RF calculation, which allows to assess the effect of the GHG background on the diagnosed forcing.

Additionally, for the calculation of instantaneous RFs diagnostic calls with a "switched" radiation scheme have been performed. This means that the radiation scheme driving the simulation and the radiation scheme used in a diagnostic call are different. For example, calls 13 and 14 from the EMAC-E5rad-pi simulation can be used to evaluate the instantaneous RF of present-day CO_2 using the PSrad radiation scheme in a pre-industrial simulation, which is driven by E5rad. This provides the opportunity to further assess the dependence of the RF results on the background (here this does not refer to present-day vs. pre-industrial but rather the different meteorological climatologies from the models that serve as different backgrounds) or the

[2] We denote all flux changes resulting from perturbations of GHGs with RF, although RF is often recommended for use with respect to the pre-industrial reference state, especially within the CMIP framework (Pincus et al., 2016), in order to ensure optimal comparability in multi-model intercomparison studies as e.g. by Ceppi et al. (2017) and Zelinka et al. (2020). We follow the less strict definition of Fuglestvedt et al. (e.g 2010) and Ramaswamy et al. (2018), according to which the use of any quasi-stationary reference state is appropriate. This notion emphasizes the role of RF as a predictor of expected global mean equilibrium surface temperature change (e.g. Hansen et al., 2005).

employed radiation scheme.

Table 4. Employed radiation perturbations for the four EMAC simulations. The first call drives the respective simulation, calls 02–12 are used for calculating various instantaneous RFs due to the perturbation of GHGs. Calls 13–23 allow to assess the RFs of the same perturbation with the switched radiation scheme, whereas calls 24–34 allow to assess the stratospheric adjusted RFs.

Call	EMAC-E5rad-pi	EMAC-E5rad-pd	EMAC-PSrad-pi	EMAC-PSrad-pd
01	base	base	base	base
02-23	instantaneous			
02/13*	base	base	base	base
03/14	CO_2(pd)	CO_2-pi	CO_2(pd)	CO_2-pi
04/15	N_2O(pd)	N_2O(pi)	N_2O(pd)	N_2O(pi)
05/16	CH_4(pd)	CH_4(pi)	CH_4(pd)	CH_4(pi)
06/17	CFC(pd)	CFC(pi)	CFC(pd)	CFC(pi)
07/18	2xCO_2(pi)	2xCO_2(pd)	2xCO_2(pi)	2xCO_2(pd)
08/19	4xCO_2(pi)	4xCO_2(pd)	4xCO_2(pi)	4xCO_2(pd)
09/20	2xCH_4(pi)	2xCH_4(pd)	2xCH_4(pi)	2xCH_4(pd)
10/21	5xCH_4(pi)	5xCH_4(pd)	5xCH_4(pi)	5xCH_4(pd)
11/22	2xN_2O(pi)	2xN_2O(pd)	2xN_2O(pi)	2xN_2O(pd)
12/23	5xN_2O(pi)	5xN_2O(pd)	5xN_2O(pi)	5xN_2O(pd)
24-34	stratospheric adjusted			
24	base	base	base	base
25	CO_2(pd)	CO_2(pi)	CO_2(pd)	CO_2(pi)
26	N_2O(pd)	N_2O(pi)	N_2O(pd)	N_2O(pi)
27	CH_4(pd)	CH_4(pi)	CH_4(pd)	CH_4(pi)
28	CFC(pd)	CFC(pi)	CFC(pd)	CFC(pi)
29	2xCO_2(pi)	2xCO_2(pd)	2xCO_2(pi)	2xCO_2(pd)
30	4xCO_2(pi)	4xCO_2(pd)	4xCO_2(pi)	4xCO_2(pd)
31	2xCH_4(pi)	2xCH_4(pd)	2xCH_4(pi)	2xCH_4(pd)
32	5xCH_4(pi)	5xCH_4(pd)	5xCH_4(pi)	5xCH_4(pd)
33	2xN_2O(pi)	2xN_2O(pd)	2xN_2O(pi)	2xN_2O(pd)
34	5xN_2O(pi)	5xN_2O(pd)	5xN_2O(pi)	5xN_2O(pd)

∗ first number refers to the call with the driving radiation scheme, second number to the call with the switched radiation scheme.

Table 5 shows the instantaneous and stratospheric adjusted RF means for the last 10 years of the simulation for different GHG perturbations. In the calls in which a single GHG is doubled, quadrupled or quintupled, the increase relates to the
610 respective base period of the simulations, i.e. for the 2xCH_4 experiments the CH_4(pi) values have been doubled for the pi

simulations, whereas the CH_4(pd) values have been doubled for the pd simulations. Note that in this table the forcings are calculated with the same radiation scheme that is also driving the ~~dynamic~~ GCM-type simulation. For instantaneous RFs, we will also address (somewhat below) the results from RF calculations, which result from switching the radiation scheme (Tab. 7).

We start our evaluation by comparing stratospheric adjusted RFs from our simulations (columns 2 to 5 in Table 5) with idealized estimates (two rightmost columns in Table 5), which are based on formulas presented by Etminan et al. (2016). Overall the results from the simulations using PSrad are closer to the Etminan-based estimates concerning stratospheric adjusted RF. In particular, this is true for the assessment of stratospheric adjusted RFs from CH_4(pi) and 2xCH_4, which are substantially higher in PSrad than in E5rad, and for 4xCO_2, which are lower in PSrad than in E5rad. We note here that the estimates given in brackets are outside the recommended range of the formulas as indicated by Etminan et al. (2016). We nevertheless present these values as they provide additional evidence that the PSrad scheme yields much more realistic stratospheric adjusted RF values, especially for CH_4 and (see below) N_2O perturbations. The instantaneous and stratospheric adjusted RF values due to doubling or quadrupling CO_2 from the EMAC-E5rad-pd simulation are in agreement with previous results obtained with EMAC and the ECHAM5 radiation scheme as presented by Dietmüller et al. (2014) and Rieger et al. (2017; see the forward results in both studies).

Additional stratospheric adjusted and instantaneous RFs for 2xCO_2 and 3xCH_4 from global model simulations have been presented by Richardson et al. (2019). Please see their Section 2 on how the respective forcings were defined and note that they (mostly but not exclusively) use present-day as the reference state. For the latter reason, we will address results from our pd simulations for comparisons only. For the 2xCO_2 RFs, the results from our EMAC-PSrad-pd simulation are closer to the values presented by Richardson et al. (2019) than the RFs based on EMAC-E5rad-pd for both instantaneous and stratospheric adjusted RFs. For 3xCH_4 RFs the results from our EMAC-E5rad-pd simulation (0.24 W m^{-2} and 0.3 W m^{-2} for instantaneous RF and stratospheric adjusted RF, respectively; interpolated from the 2xCH_4 and 5xCH_4 RFs) show clearly lower values than the results from the EMAC-PSrad-pd simulation (0.97 W m^{-2} and 0.95 W m^{-2}, respectively; interpolated as before). The increased RFs associated with a 3xCH_4 experiment as diagnosed from PSrad are in better agreement with the values presented by Richardson et al. (2019), which are somewhat above 1 W m^{-2}.

Another aspect to note about the methane RFs is that with ~~PSrad~~ E5rad the stratospheric temperature adjustment acts to ~~reduce~~ increase the RF in comparison ~~with~~ to the instantaneous RF, whereas for ~~E5rad it acts to increase it~~PSrad the differences between instantaneous and stratospheric adjusted RF are smaller and the sign depends on the background state. PSrad includes SW absorption of methane in two bands in the near-infrared (3.08 - 3.85 μm and 2.15 - 2.50 μm; cf. the RRTM bands described in the ECHAM6 documentation Giorgetta et al., 2013b). The SW absorption acts to counteract the stratospheric cooling induced by the LW radiation (Byrom and Shine, 2022, their Fig. 2). ~~Similarly, Smith et al. (2018, their Fig. S6) found~~ Hence, the adjustment difference we find between PSrad and E5rad is in part consistent with the results from Smith et al. (2018, their Fig. S6). They point out that for the same experiments as analysed by Richardson et al. (2019), the rapid radiative adjustment induced

by the stratospheric temperature adjustment is negative in models with the explicit treatment of methane SW absorption in the radiation scheme, and positive in models without. However, in the latter case the increase reported by Smith et al. (2018) is more pronounced as there is a substantial additional contribution from cloud radiative adjustments that are not covered by our technique.

The instantaneous RF of 3xN_2O with respect to present-day conditions has been assessed by Hodnebrog et al. (2020) for global models and LBL calculations. They find an instantaneous RF of roughly 1.5 W m^{-2} and 1.4 W m^{-2}, respectively. Interpolation of the instantaneous 2xN_2O and 5xN_2O calculations from EMAC-E5rad-pd and EMAC-PSrad-pd yields values of 2.49 W m^{-2} and 1.37 W m^{-2}, respectively, clearly emphasizing the superiority of N_2O forcings provided by the latter.

Table 6 shows the global mean clear-sky instantaneous RFs corresponding to the all-sky instantaneous RFs presented in Table 5. Our results can be compared with those from Pincus et al. (2020), which were derived from the multi-model mean of so-called "benchmark" models. Based on the description by Pincus et al. (2020), we can compare the results from EMAC-E5rad-pd and EMAC-PSrad-pd shown in Table 6 with their results for clear-sky instantaneous RF due to increasing a single GHG from pre-industrial to present-day values. However, as the base periods and values for pi and pd conditions are different, for example, Pincus et al. (2020) use 2014 as pd, we rescaled our clear-sky RF results to allow for a better comparison. The corresponding values are listed in brackets in Table 6. For the rescaling, we assumed that the 2014 values used by Pincus et al. (2020) are similar to the values presented by Meinshausen et al. (2017). Consequently, the clear-sky instantaneous RFs were adjusted as follows: $iRF^*_{cs} = iRF_{cs} \cdot \Delta X_{P20}/\Delta X_{N23}$, where iRF_{cs} refers to the instantaneous clear-sky RF and the asterisk denotes the corresponding rescaled quantity. ΔX denotes the change (in mol mol^{-1}) of the species X from pi to pd conditions and the subscripts P20 and N23 refer to Pincus et al. (2020) and our study, respectively. Taking into account the rescaling, all clear-sky RFs for the pi experiments calculated with PSrad are closer to the results presented by Pincus et al. (2020) than the results obtained with E5rad. As an example, the global mean clear-sky RF (including the above-mentioned correction) due to the rise of methane from pi to pd increases from 0.41 W m^{-2} in the E5rad simulation to 0.51 W m^{-2} in the simulation with PSrad and is closer to the reference value of 0.67 W m^{-2} presented by Pincus et al. (2020). Conversely, for N_2O the clear-sky instantaneous RF decreases when PSrad is used and is thus in better agreement with the value of approximately 0.21 W m^{-2} presented by Pincus et al. (2020).

Pincus et al. (2020) also show clear-sky RFs with respect to CO_2-folding experiments. Presuming that they use pre-industrial CO_2 as a reference state for CO_2, whereas the other GHGs and the meteorology are representative of present-day conditions, one can try to compare their results with our rescaled results for the CO_2-folding experiments performed in the EMAC-E5rad-pi and EMAC-PSrad-pi simulations. This would lead to a seemingly better agreement of E5rad than PSrad results with their values. However, we warrant that this comparison is questionable due to the following: (i) We have a different GHG (including water vapour) background, namely pi, in comparison to their background of pd conditions. We assume that through saturation we would get lower RFs (i.e. a reduced sensitivity to CO_2 changes) than presented here, if the CO_2-folding would have been

Table 5. RFs ($W\,m^{-2}$) for perturbations based on the diagnostic radiation calls described in Table 4 for the last 10 years of the simulations. In addition best estimates based on the formula from Etminan et al. (2016) are given as reference values for stratospheric adjusted RF.

	EMAC-E5rad-pi	EMAC-E5rad-pd	EMAC-PSrad-pi	EMAC-PSrad-pd	Etminan pi	Etminan pd
Perturbation	instantaneous RF ($W\,m^{-2}$)					
CO_2(pi)	0.86	0.94	0.75	0.81		
N_2O(pi)	0.22	0.21	0.19	0.16		
CH_4(pi)	0.24	0.25	0.41	0.39		
CFC(pi)	0.24	0.25	0.29	0.29		
2xCO_2	2.34	2.65	1.93	2.13		
4xCO_2	5.04	5.77	3.85	4.24		
2xCH_4	0.21	0.16	0.35	0.58		
5xCH_4	0.42	0.39	1.15	1.75		
2xN_2O	1.34	1.41	1.03	0.87		
5xN_2O	4.44	4.65	2.64	2.37		
Perturbation	stratospheric adjusted RF ($W\,m^{-2}$)					
CO_2(pi)	1.44	1.45	1.38	1.39	1.40	1.39
N_2O(pi)	0.23	0.21	0.20	0.17	0.14	0.13
CH_4(pi)	0.29	0.29	0.42	0.38	0.53	0.53
CFC(pi)	0.23	0.25	0.27	0.27	-	-
2xCO_2	4.02	4.23	3.80	3.91	3.80	3.83
4xCO_2	8.61	9.12	7.88	8.07	7.96	8.04
2xCH_4	0.26	0.20	0.36	0.57	0.46	(0.64)
5xCH_4	0.54	0.50	1.16	1.70	(1.32)	(1.74)
2xN_2O	1.38	1.45	1.08	0.92	(0.77)	(0.79)
5xN_2O	4.62	4.83	2.78	2.50	(2.33)	(2.40)

The interannual standard deviations were in the order of 0.01 $W\,m^{-2}$. Values in brackets in the columns Etminan-pi and Etminan-pd are for perturbations that are outside the valid range of the approximation formulas given by Etminan et al. (2016). The perturbations 2xN_2O(pi) and 2xCH_4(pd) are close to the valid range.

performed against a pd GHG background. (ii) In the climatological pd background, the tropospheric temperatures are likely higher ~~than~~ and the stratospheric temperatures lower than for our pi background. Here, we reason that ~~this~~ both changes will likely lead to an increased RF as diagnosed from CO_2-folding experiments, ~~as the surface emits more LW radiation which can be attenuated by the additional CO_2~~with the stratospheric component potentially making the larger contribution (He et al., 2023).

An estimate of the combined effect can be obtained when comparing our "forward" and "backward" experiments for calculating the clear-sky RF due to the increase of a single GHG from pi to pd levels. For both, E5rad and PSrad, the clear-sky RF

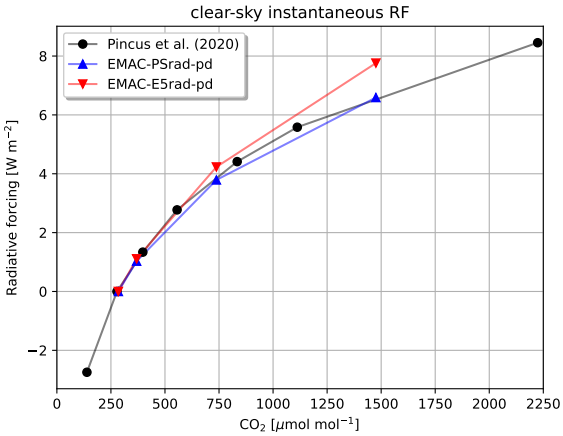

Figure 10. Clear-sky instantaneous RF for CO_2-folding experiments from our pd simulations compared to benchmark values from Pincus et al. (2020). The reference background is given by pd-conditions, which slightly differ between our study and the study by Pincus et al. (2020). Further for the pd conditions of Pincus et al. (2020) in 2014 we assumed the respective values according to Meinshausen et al. (2017; see text for details). Note that clear-sky instantaneous RF is calculated with respect to a pd background for all non-CO_2 greenhouse gases and pi-conditions for CO_2.

due to the rise of CO_2 from pi to pd levels is higher, when assessed against the pd background. For N_2O the relation is reversed, whereas for CFCs there is (almost) no dependence of the instantaneous clear-sky RF on the background. Interestingly, for CH_4 the clear-sky instantaneous RFs are higher for a pd background when assessed with E5rad, and lower when assessed with PSrad compared to the RFs when calculated against a pi background. Qualitatively similar dependencies of the instantaneous RFs on the GHG background are found for the all-sky fluxes (see Table 5).

Alternatively, for the comparison of clear-sky CO_2 RFs with the benchmark results presented by Pincus et al. (2020) we can also employ the CO_2-folding experiments from our pd-background simulations. This has the advantage that the background with respect to which RF of CO_2-folding experiments is calculated is comparable between the studies. However, it comes at the drawback that the sampling points with respect to which CO_2-folding RFs are determined differ. Figure 10 shows the corresponding results, which indicate that the EMAC-E5rad-pd simulation does not show better clear-sky instantaneous RFs compared to EMAC-PSrad-pd simulation. In particular for extreme CO_2-folding experiments, the simulation with PSrad seems to produce better results than the simulation with E5rad.

The instantaneous RFs presented in Table 5 are complemented by Table 7, which arises when the instantaneous RF is calculated with a different radiation scheme compared to the scheme that is driving the simulation. Hence, the columns of Table 5 and Table 7 can be compared to each other one to one. Overall the relative differences are roughly 10% or less, showing that the results are relatively robust to changes in the background state related to switching the radiation scheme. With respect to experiments, that assess the instantaneous RF due to an increase of a single GHG from pi to pd levels, we find that the changes

Table 6. Global mean clear-sky instantaneous RFs ($W\,m^{-2}$) for perturbations based on the diagnostic radiation calls described in Table 4 for the last 10 years of the simulations. Values in brackets denote rescaled EMAC clear-sky RFs, which are supposed to ensure better comparability with the RFs presented by Pincus et al. (2020). See text for details.

	EMAC-E5rad-pi	EMAC-E5rad-pd	EMAC-PSrad-pi	EMAC-PSrad-pd
Perturbation	clear-sky instantaneous RF ($W\,m^{-2}$)			
CO_2(pi)	1.04	1.11 (1.57)	0.97	1.03 (1.46)
N_2O(pi)	0.27	0.25 (0.32)	0.24	0.19 (0.24)
CH_4(pi)	0.33	0.35 (0.41)	0.48	0.44 (0.51)
CFC(pi)	0.33	0.34 (0.43)	0.38	0.38 (0.48)
2xCO_2	2.81	3.12	2.55	2.76
4xCO_2	5.96	6.65	5.17	5.56
2xCH_4	0.30	0.23	0.41	0.67
5xCH_4	0.60	0.54	1.34	2.01
2xN_2O	1.63	1.70	1.27	1.07
5xN_2O	5.37	5.59	3.27	2.93

The interannual standard deviations were in the order of 0.01 $W\,m^{-2}$.

of the meteorological background associated with the radiation scheme do not play a major role: For CFCs, N_2O and CH_4 they are almost negligible whereas they are somewhat larger for CO_2 (the respective values in Table 5 and Table 7 are almost identical except for the CO_2 perturbations).

Related to the dependence of RFs for CO_2 perturbations on the background, we have previously detected a larger CO_2 sensitivity in the E5rad compared to the PSrad simulations. As discussed above for the dependence of the instantaneous CO_2 RFs on the pi and pd background, we point out that a warmer stratosphere in the PSrad compared to the E5rad simulations might be contributing to the lower RF values diagnosed from PSrad compared to E5rad. In line with this argument, instantaneous all-sky CO_2 RFs increase (decrease) for E5rad (PSrad) when the background is provided by the switched radiation scheme PSrad (E5rad) as can be seen from the comparison of Tables 5 and 7.

Table 7. Instantaneous RFs for perturbations described in Table 4 for the last 10 years of the simulations, where the radiation scheme for diagnosing the instantaneous RF was switched compared to the radiation scheme driving the simulation. As an example: in the second column radiation calls with the E5rad scheme were used to calculate the instantaneous RFs within the EMAC-PSrad-pi simulation.

Simulation	EMAC-PSrad-pi	EMAC-PSrad-pd	EMAC-E5rad-pi	EMAC-E5rad-pd
Radiation scheme	E5rad	E5rad	PSrad	PSrad
Perturbation	instantaneous RF ($W\,m^{-2}$)			
CO_2(pi)	*0.81*	*0.89*	*0.80*	*0.86*
N_2O(pi)	*0.22*	*0.21*	*0.20*	*0.16*
CH_4(pi)	*0.24*	*0.26*	*0.42*	*0.39*
CFC(pi)	*0.24*	*0.25*	*0.29*	*0.29*
2xCO_2	*2.19*	*2.50*	*2.08*	*2.28*
4xCO_2	*4.72*	*5.45*	*4.18*	*4.58*
2xCH_4	*0.22*	*0.16*	*0.36*	*0.59*
5xCH_4	*0.42*	*0.38*	*1.18*	*1.78*
2xN_2O	*1.32*	*1.38*	*1.04*	*0.88*
5xN_2O	*4.35*	*4.56*	*2.67*	*2.40*

The interannual standard deviations were in the order of 0.01 $W\,m^{-2}$

5 Summary and conclusions

In this paper, we describe the recent upgrades of the MESSy radiation infrastructure and its first applications. In Sect. 2 we give a detailed overview of the implemented changes. A ~~guideline~~ guiding principle through the implementation process has been to retain the possibility to use all previous model setups (backward compatibility) and to ensure the applicability of MESSy-specific features (e.g. multiple radiation calls) also with the updated radiation infrastructure. Specific highlights of the new implementations are the integration of the radiation scheme PSrad and the availability of a new submodel ALBEDO, which features solar zenith angle dependent albedos. Further, a white-sky albedo for snow-free land has been compiled based on satellite data.

The third Section (Sect. 3.2) exemplarily describes the model optimization of a typical "old" (with ECHAM5 radiation) and "new" (with PSrad radiation) ~~dynamical model~~ GCM-type setup (fixed sea surface temperatures and no chemistry except for simplified methane chemistry) with a consistent set of parameters for pre-industrial and present-day conditions. Comparing the old and new setup, also with observational and reanalysis data, shows that the main features of the simulated climate (also known from previous ECHAM5 and other ECHAM6.1 simulations, e.g. Stevens et al., 2013) remain. However, some biases of the old model setup, e.g. the cold bias in the tropical upper troposphere–lower stratosphere and a too weak polar vortex ~~,~~ ~~seem to be~~ in the southern hemisphere winter, are reduced when the PSrad scheme is employed.

Finally, we show radiative forcing results based on the old and the new model setups using multiple diagnostic radiation calls. In total we perform 33 additional diagnostic radiation calls per simulation to assess various radiative forcings. In particular, we show stratospheric (temperature) adjusted and instantaneous RF values due to reduced or increased greenhouse gases. When comparing these results with previous estimates, we find that PSrad generally performs better for instantaneous and stratospheric-adjusted radiative forcings. In particular, methane (nitrous oxide) radiative forcings calculated with PSrad are much increased (decreased) in comparison to the radiative forcings calculated with the ECHAM5 radiation scheme, which means a clear improvement when compared to benchmark results. For the instantaneous forcings we also derive results where the radiation scheme of the diagnostic calls is switched compared to the driving radiation scheme, i.e. using the old radiation scheme to propagate the simulation and evaluating two additional diagnostic radiation calls with the new radiation scheme to determine the instantaneous flux changes or vice versa. It appears that changes in the radiative forcing results from the previous (ECHAM5) setup to the new (PSrad) setup are mainly attributable to the radiative transfer calculations themselves, whereas the changed background climatology related to the driving radiation scheme plays only a minor role.

The implemented changes lead to an improved representation of tropical upper tropospheric temperatures (and thus stratospheric water vapour). Further, various radiative forcings due to greenhouse gas perturbations tend to be improved. In particular, this is the case for methane forcing experiments, which show a higher radiative forcing with the new radiation scheme, PSrad, and are thus in better agreement with literature-based reference values. The latter can be exploited to better quantify methane

radiative forcings and the role of methane as a feedback component in the climate system. The developments mark an important step for the MESSy framework to be able to include additional radiation schemes. The next steps concerning the use of the MESSy radiation infrastructure are to employ the PSrad scheme with interactive chemistry and an online coupled ocean (Earth system model setup). Further envisaged developments are the coupling of PSrad to FUBrad and the use of PSrad with an interactive aerosol model, which will be enabled by the revision of the AEROPT submodel.

References (DOIs) for MESSy have been added as requested by the executive editor.

Code availability. The Modular Earth Submodel System (MESSy; doi: 10.5281/zenodo.8360186) is continuously further developed and applied by a consortium of institutions. The usage of MESSy and access to the source code is licenced to all affiliates of institutions which are members of the MESSy Consortium. Institutions can become a member of the MESSy Consortium by signing the MESSy Memorandum of Understanding. More information can be found on the MESSy Consortium Website (http://www.messy-interface.org). The code presented here is based on MESSy version 2.55 (The MESSy Consortium, 2021) and is archived as The MESSy Consortium (2023). The developments will also be available in the next official release (version 2.56).

Data availability. GPCP v2.3 data were downloaded from https://psl.noaa.gov/data/gridded/data.gpcp.html (downloaded 15 February 2023, last access 17 February 2023). MODIS MCD43GF v006 data (MODIS/Terra+Aqua BRDF/Albedo Gap-Filled Snow-Free Daily L3 Global 30ArcSec CMG) from the NASA EOSDIS Land Processes Distributed Active Archive Center (LP DAAC; Schaaf, 2019) located at the USGS Earth Resources Observation and Science (EROS) Center have been obtained from the Data Pool (https://e4ftl01.cr.usgs.gov/MOTA/MCD43GF.006). HadISST data were obtained from https://www.metoffice.gov.uk/hadobs/hadisst/ and are © British Crown Copyright, Met Office, [2023], provided under a Non-Commercial Government Licence http://www.nationalarchives.gov.uk/doc/non-commercial-government-licence/version/2/. Contains modified Copernicus Climate Change Service information [2023]. Neither the European Commission nor ECMWF is responsible for any use that may be made of the Copernicus information or data it contains. ERA5 monthly mean data on pressure levels (Hersbach et al., 2023) were downloaded from the Copernicus Climate Change Service (C3S) Climate Data Store (Copernicus Climate Change Service, Climate Data Store, 2023). Various CMIP6 data (e.g. Meinshausen and Vogel, 2016; Matthes et al., 2017b; ETH Zürich (ETHZ), 2017) used as boundary conditions (also for previous EMAC simulations) are available from ESGF.

Author contributions. MN implemented RAD/CLOUDOPT with help of PJ and LS. LS and PJ implemented the ALBEDO submodel with the help of FW and MN. LS adjusted AEROPT with the help of PJ and MN. Preparation of model setups for parameter optimization and evaluation: LS, MN, PJ, PG, MK and FW. Conduction of simulations: LS. Data analysis: LS, FW and MN. MN drafted and wrote main parts of the paper with help of LS, FW and MP. All authors contributed to the discussion of the results and/or to the developments described in the paper.

Competing interests. At least one of the (co-)authors is a member of the editorial board of Geoscientific Model Development. The authors have no other competing interests to declare.

Acknowledgements. We thank two anonymous reviewers and the editor for their thoughtful remarks, which lead to an improvement of the manuscript. We are thankful for helpful clarifications from Sebastian Rast (MPI-M) regarding various ICON and ECHAM related topics. We thank Ralf Meerkötter (DLR) for pointing out the importance of the SZA dependence of the surface albedos, Birgit Hassler (DLR) for the internal review, Mattia Righi (DLR) for assistance and helpful comments regarding the optimization procedure, and the EVA department at DLR for help with the ESMValTool. We thank Simone Dietmüller (DLR) for helpful discussions on stratospheric adjusted radiative forcing and Bernhard Mayer (LMU) for helpful discussions e.g. on methane radiative forcing. The analysis of simulation results was supported by the ESMValTool 2.8 (doi:10.5281/zenodo.3401363) and ESMValCore 2.8 (doi:10.5281/zenodo.3387139) (Righi et al., 2020). We used Climate Data Operators (CDO; https://code.mpimet.mpg.de/projects/cdo/, last access: 21 August 2023; Schulzweida, 2022) for data processing and the NCAR Command Language (NCL, 2019, see references) for parts of the data analysis. Global Precipitation Climatology Project (GPCP) Monthly Analysis Product data were provided by the NOAA PSL, Boulder, Colorado, USA, from their website at https://psl.noaa.gov (last access 17 February 2023). We thank the NASA EOSDIS Land Processes Distributed Active Archive Center (LP DAAC) for making MODIS MCD43GFv006 data available (Schaaf, 2019). HadISST data (Rayner et al., 2003) are available from www.metoffice.gov.uk/hadobs (last access 06 Mar 2023). We acknowledge the World Climate Research Programme, which, through its Working Group on Coupled Modelling, coordinated and promoted CMIP6. We thank the climate modeling groups for producing and making available their model output, the Earth System Grid Federation (ESGF) for archiving the data and providing access, and the multiple funding agencies who support CMIP6 and ESGF. The simulations have been performed on the DLR HPC-cluster CARA.

Financial support. The work described in this paper has received funding from the Initiative and Networking Fund of the Helmholtz Association through the project “Advanced Earth System Modelling Capacity (ESM)” and from the Helmholtz Association project “Joint Lab Exascale Earth System Modelling (JL-ExaESM)”. The content of the paper is the sole responsibility of the author(s) and it does not represent the opinion of the Helmholtz Association, and the Helmholtz Association is not responsible for any use that might be made of the information contained. Further funding was received from the DFG through the project IRFAM-ClimS (Vorhaben WI 5369/1-1). PG acknowledges funding from the German Federal Ministry of Education and Research (BMBF) as part of the "Research for Sustainability (FONA)" strategy for the project entitled "The Climate Model Intercomparison Project 6 - Chemistry (CMIP6-Chemistry, Förderkennzeichen 01LP1606A).

References

Adler, R., Huffman, G., Chang, A., Ferraro, R., Xie, P., Janowiak, J., Rudolf, B., Schneider, U., Curtis, S., Bolvin, D., Gruber, A., Susskind, J., and Arkin, P.: The Version 2 Global Precipitation Climatology Project (GPCP) Monthly Precipitation Analysis (1979-Present), J. Hydrometeorol., 4, 1147–1167, https://doi.org/10.1175/1525-7541(2003)004<1147:TVGPCP>2.0.CO;2, 2003.

Adler, R. F., Sapiano, M. R. P., Huffman, G. J., Wang, J.-J., Gu, G., Bolvin, D., Chiu, L., Schneider, U., Becker, A., Nelkin, E., Xie, P., Ferraro, R., and Shin, D.-B.: The Global Precipitation Climatology Project (GPCP) Monthly Analysis (New Version 2.3) and a Review of 2017 Global Precipitation, Atmosphere, 9, https://doi.org/10.3390/atmos9040138, 2018.

Briegleb, B. P.: Delta-Eddington approximation for solar radiation in the NCAR community climate model, Journal of Geophysical Research: Atmospheres, 97, 7603–7612, https://doi.org/10.1029/92JD00291, 1992.

Brinkop, S., Dameris, M., Jöckel, P., Garny, H., Lossow, S., and Stiller, G.: The millennium water vapour drop in chemistry–climate model simulations, Atmospheric Chemistry and Physics, 16, 8125–8140, https://doi.org/10.5194/acp-16-8125-2016, 2016.

Burkholder, J. B.: Summary of abundances, lifetimes, ozone depletion potentials (ODPs), radiative efficiencies (REs), global warming potentials (GWPs), and global temperature change potentials (GTPs), Appendix A in Scientific Assessment of Ozone Depletion: 2018, Global Ozone Research and Monitoring Project–Report No. 58, World Meteorological Organization, Geneva, Switzerland, 2018.

Byrom, R. E. and Shine, K. P.: Methane's Solar Radiative Forcing, Geophysical Research Letters, 49, e2022GL098 270, https://doi.org/10.1029/2022GL098270, 2022.

Carpenter, L. J., Daniel, J., Fleming, E., Hanaoka, T., Hu, J., Ravishankara, A. R., Ross, M. N., Tilmes, S., Wallington, T. J., and Wuebbles, D. J.: Scenarios and information for policymakers, Chapter 6 in Scientific Assessment of Ozone Depletion: 2018, Global Ozone Research and Monitoring Project–Report No. 58, World Meteorological Organization, Geneva, Switzerland, 2018.

Ceppi, P., Brient, F., Zelinka, M. D., and Hartmann, D. L.: Cloud feedback mechanisms and their representation in global climate models, WIREs Climate Change, 8, e465, https://doi.org/10.1002/wcc.465, 2017.

CERES Science Team: CERES_EBAF_Ed4.1 Data Quality Summary, Version 3, https://ceres.larc.nasa.gov/documents/DQ_summaries/CERES_EBAF_Ed4.1_DQS.pdf, 2021.

Colman, R. A. and McAvaney, B. J.: A study of general circulation model climate feedbacks determined from perturbed sea surface temperature experiments, Journal of Geophysical Research: Atmospheres, 102, 19 383–19 402, https://doi.org/10.1029/97JD00206, 1997.

Copernicus Climate Change Service, Climate Data Store: ERA5 monthly averaged data on pressure levels from 1940 to present, Copernicus Climate Change Service (C3S) Climate Data Store (CDS), accessed 06/07-JUL-2023, https://doi.org/10.24381/cds.6860a573, 2023.

Cordero, R. R., Feron, S., Sepúlveda, E., Damiani, A., Carrera, J. M., Jorquera, J., Alfonso, J. A., Fuenzalida, R., Rivas, M., MacDonell, S., Seckmeyer, G., Wang, C., Ouyang, Z., and Lhermitte, S.: Evaluation of MODIS-derived estimates of the albedo over the Atacama Desert using ground-based spectral measurements, Scientific Reports, 11, 19 822, https://doi.org/10.1038/s41598-021-98622-4, 2021.

Dietmüller, S., Ponater, M., and Sausen, R.: Interactive ozone induces a negative feedback in CO2-driven climate change simulations, Journal of Geophysical Research: Atmospheres, 119, 1796–1805, https://doi.org/10.1002/2013JD020575, 2014.

Dietmüller, S., Jöckel, P., Tost, H., Kunze, M., Gellhorn, C., Brinkop, S., Frömming, C., Ponater, M., Steil, B., Lauer, A., and Hendricks, J.: A new radiation infrastructure for the Modular Earth Submodel System (MESSy, based on version 2.51), Geoscientific Model Development, 9, 2209–2222, https://doi.org/10.5194/gmd-9-2209-2016, 2016.

Ebert, E. E. and Curry, J. A.: A parameterization of ice cloud optical properties for climate models, Journal of Geophysical Research: Atmospheres, 97, 3831–3836, https://doi.org/10.1029/91JD02472, 1992.

Eichinger, R. and Jöckel, P.: The generic MESSy submodel TENDENCY (v1.0) for process-based analyses in Earth system models, Geoscientific Model Development, 7, 1573–1582, https://doi.org/10.5194/gmd-7-1573-2014, 2014.

ETH Zürich (ETHZ): input4MIPs.IACETH.aerosolProperties.CMIP.IACETH-SAGE3lambda-3-0-0, Earth System Grid Federation, VERSION YYYYMMDD, https://doi.org/10.22033/ESGF/input4MIPs.1681, 2017.

Etminan, M., Myhre, G., Highwood, E. J., and Shine, K. P.: Radiative forcing of carbon dioxide, methane, and nitrous oxide: A significant revision of the methane radiative forcing, Geophysical Research Letters, 43, 12,614–12,623, https://doi.org/10.1002/2016GL071930, 2016.

Eyring, V., Lamarque, J.-F., Hess, P., Arfeuille, F., Bowman, K., Chipperfield, M., Duncan, B., Fiore, A., Gettelman, A., Giorgetta, M., Granier, C., Hegglin, M., Kinnison, D., Kunze, M., Langematz, U., Luo, B., Martin, R., Matthes, K., Newman, P., Peter, T., Robock, A., Ryerson, A., Saiz-Lopez, A., Salawitch, R., Schultz, M., Shepherd, T., Shindell, D., Stähelin, J., Tegtmeier, S., Thomason, L., Tilmes, S., Vernier, J.-P., Waugh, D., and Young, P.: Overview of IGAC/SPARC Chemistry-Climate Model Initiative (CCMI) Community Simulations in Support of Upcoming Ozone and Climate Assessments, SPARC Newsletter, 40, 48–66, http://www.sparc-climate.org/fileadmin/customer/6_Publications/Newsletter_PDF/40_SPARCnewsletter_Jan2013_web.pdf, last access 6 August 2017, 2013.

Eyring, V., Bony, S., Meehl, G. A., Senior, C. A., Stevens, B., Stouffer, R. J., and Taylor, K. E.: Overview of the Coupled Model Intercomparison Project Phase 6 (CMIP6) experimental design and organization, Geoscientific Model Development, 9, 1937–1958, https://doi.org/10.5194/gmd-9-1937-2016, 2016.

Fouquart, Y. and Bonnel, B.: Computations of solar heating of the Earth's atmosphere: A new parameterization, Beitr. Phys. Atmos., 53, 35–62, 1980.

Fuglestvedt, J., Shine, K., Berntsen, T., Cook, J., Lee, D., Stenke, A., Skeie, R., Velders, G., and Waitz, I.: Transport impacts on atmosphere and climate: Metrics, Atmospheric Environment, 44, 4648–4677, https://doi.org/10.1016/j.atmosenv.2009.04.044, transport Impacts on Atmosphere and Climate: The ATTICA Assessment Report, 2010.

Giorgetta, M. A., Jungclaus, J., Reick, C. H., Legutke, S., Bader, J., Böttinger, M., Brovkin, V., Crueger, T., Esch, M., Fieg, K., Glushak, K., Gayler, V., Haak, H., Hollweg, H.-D., Ilyina, T., Kinne, S., Kornblueh, L., Matei, D., Mauritsen, T., Mikolajewicz, U., Mueller, W., Notz, D., Pithan, F., Raddatz, T., Rast, S., Redler, R., Roeckner, E., Schmidt, H., Schnur, R., Segschneider, J., Six, K. D., Stockhause, M., Timmreck, C., Wegner, J., Widmann, H., Wieners, K.-H., Claussen, M., Marotzke, J., and Stevens, B.: Climate and carbon cycle changes from 1850 to 2100 in MPI-ESM simulations for the Coupled Model Intercomparison Project phase 5, Journal of Advances in Modeling Earth Systems, 5, 572–597, https://doi.org/10.1002/jame.20038, 2013a.

Giorgetta, M. A., Roeckner, E., Mauritsen, T., Bader, J., Crueger, T., Esch, M., Rast, S., Kornblueh, L., Schmidt, H., Kinne, S., Hohenegger, C., Möbis, B., Krismer, T., Wieners, K., and Stevens, B.: The atmospheric general circulation model ECHAM6 - Model description, Reports on Earth System Science / Max-Planck-Institut für Meteorologie, 135, https://doi.org/10.17617/2.1810480, 2013b.

Giorgetta, M. A., Brokopf, R., Crueger, T., Esch, M., Fiedler, S., Helmert, J., Hohenegger, C., Kornblueh, L., Köhler, M., Manzini, E., Mauritsen, T., Nam, C., Raddatz, T., Rast, S., Reinert, D., Sakradzija, M., Schmidt, H., Schneck, R., Schnur, R., Silvers, L., Wan, H., Zängl, G., and Stevens, B.: ICON-A, the Atmosphere Component of the ICON Earth System Model: I. Model Description, Journal of Advances in Modeling Earth Systems, 10, 1613–1637, https://doi.org/10.1029/2017MS001242, 2018.

Hagemann, S.: An improved land surface parameter dataset for global and regional climate models, Report / Max-Planck-Institut für Meteorologie, 336, https://doi.org/10.17617/2.2344576, 2002.

Hansen, J., Sato, M., Ruedy, R., Nazarenko, L., Lacis, A., Schmidt, G. A., Russell, G., Aleinov, I., Bauer, M., Bauer, S., Bell, N., Cairns, B., Canuto, V., Chandler, M., Cheng, Y., Del Genio, A., Faluvegi, G., Fleming, E., Friend, A., Hall, T., Jackman, C., Kelley, M., Kiang,

N., Koch, D., Lean, J., Lerner, J., Lo, K., Menon, S., Miller, R., Minnis, P., Novakov, T., Oinas, V., Perlwitz, J., Perlwitz, J., Rind, D., Romanou, A., Shindell, D., Stone, P., Sun, S., Tausnev, N., Thresher, D., Wielicki, B., Wong, T., Yao, M., and Zhang, S.: Efficacy of climate forcings, Journal of Geophysical Research: Atmospheres, 110, https://doi.org/10.1029/2005JD005776, 2005.

He, H., Kramer, R. J., Soden, B. J., and Jeevanjee, N.: State dependence of CO_2 forcing and its implications for climate sensitivity, Science, 382, 1051–1056, https://doi.org/10.1126/science.abq6872, 2023.

Hersbach, H., Bell, B., Berrisford, P., Hirahara, S., Horányi, A., Muñoz-Sabater, J., Nicolas, J., Peubey, C., Radu, R., Schepers, D., Simmons, A., Soci, C., Abdalla, S., Abellan, X., Balsamo, G., Bechtold, P., Biavati, G., Bidlot, J., Bonavita, M., De Chiara, G., Dahlgren, P., Dee, D., Diamantakis, M., Dragani, R., Flemming, J., Forbes, R., Fuentes, M., Geer, A., Haimberger, L., Healy, S., Hogan, R. J., Hólm, E., Janisková, M., Keeley, S., Laloyaux, P., Lopez, P., Lupu, C., Radnoti, G., de Rosnay, P., Rozum, I., Vamborg, F., Villaume, S., and Thépaut, J.-N.: The ERA5 global reanalysis, Quarterly Journal of the Royal Meteorological Society, 146, 1999–2049, https://doi.org/10.1002/qj.3803, 2020.

Hersbach, H., Bell, B., Berrisford, P., Biavati, G., Horányi, A., Muñoz-Sabater, J., Nicolas, J., Peubey, C., Radu, R., Rozum, I., Schepers, D., Simmons, A., Soci, C., Dee, D., and Thépaut, J.-N.: ERA5 monthly averaged data on pressure levels from 1940 to present, Copernicus Climate Change Service (C3S) Climate Data Store (CDS), accessed 06/07-JUL-2023, https://doi.org/10.24381/cds.6860a573, 2023.

Hodnebrog, Ø., Myhre, G., Kramer, R. J., Shine, K. P., Andrews, T., Faluvegi, G., Kasoar, M. R., Kirkevåg, A., Lamarque, J., Mülmenstädt, J., Oliviè, D., Samset, B. H., Shindell, D., Smith, C. J., Takemura, T., and Voulgarakis, A.: The effect of rapid adjustments to halocarbons and N_2O on radiative forcing, npj Climate and Atmospheric Science, 3, https://doi.org/10.1038/s41612-020-00150-x, 2020.

Hourdin, F., Mauritsen, T., Gettelman, A., Golaz, J.-C., Balaji, V., Duan, Q., Folini, D., Ji, D., Klocke, D., Qian, Y., Rauser, F., Rio, C., Tomassini, L., Watanabe, M., and Williamson, D.: The Art and Science of Climate Model Tuning, Bulletin of the American Meteorological Society, 98, 589 – 602, https://doi.org/10.1175/BAMS-D-15-00135.1, 2017.

Huffman, G. J., Adler, R. F., Arkin, P., Chang, A., Ferraro, R., Gruber, A., Janowiak, J., McNab, A., Rudolf, B., and Schneider, U.: The Global Precipitation Climatology Project (GPCP) Combined Precipitation Dataset, Bulletin of the American Meteorological Society, 78, 5 – 20, https://doi.org/10.1175/1520-0477(1997)078<0005:TGPCPG>2.0.CO;2, 1997.

Huffman, G. J., Adler, R. F., Bolvin, D. T., and Gu, G.: Improving the global precipitation record: GPCP Version 2.1, Geophysical Research Letters, 36, L17 808, https://doi.org/10.1029/2009GL040000, 2009.

Iacono, M. J., Delamere, J. S., Mlawer, E. J., Shephard, M. W., Clough, S. A., and Collins, W. D.: Radiative forcing by long-lived greenhouse gases: Calculations with the AER radiative transfer models, Journal of Geophysical Research: Atmospheres, 113, https://doi.org/10.1029/2008JD009944, 2008.

Jöckel, P.: refD1 data produced by the EMAC-CCMI2 model at MESSy-Consortium, NERC EDS Centre for Environmental Data Analysis, 17 July 2023, https://catalogue.ceda.ac.uk/uuid/9b15ae551fda4035a7940a3adbe31691, 2023.

Jöckel, P., Sander, R., Kerkweg, A., Tost, H., and Lelieveld, J.: Technical Note: The Modular Earth Submodel System (MESSy) - a new approach towards Earth System Modeling, Atmos. Chem. Phys., 5, 433–444, https://doi.org/10.5194/acp-5-433-2005, 2005.

Jöckel, P., Kerkweg, A., Pozzer, A., Sander, R., Tost, H., Riede, H., Baumgaertner, A., Gromov, S., and Kern, B.: Development cycle 2 of the Modular Earth Submodel System (MESSy2), Geoscientific Model Development, 3, 717–752, https://doi.org/10.5194/gmd-3-717-2010, 2010.

Jöckel, P., Tost, H., Pozzer, A., Kunze, M., Kirner, O., Brenninkmeijer, C. A. M., Brinkop, S., Cai, D. S., Dyroff, C., Eckstein, J., Frank, F., Garny, H., Gottschaldt, K.-D., Graf, P., Grewe, V., Kerkweg, A., Kern, B., Matthes, S., Mertens, M., Meul, S., Neumaier, M., Nützel, M., Oberländer-Hayn, S., Ruhnke, R., Runde, T., Sander, R., Scharffe, D., and Zahn, A.: Earth System Chemistry integrated Mod-

elling (ESCiMo) with the Modular Earth Submodel System (MESSy) version 2.51, Geoscientific Model Development, 9, 1153–1200, https://doi.org/10.5194/gmd-9-1153-2016, 2016.

Johnson, G. C., Lyman, J. M., and Loeb, N. G.: Improving estimates of Earth's energy imbalance, Nature Climate Change, 6, 639–640, https://doi.org/10.1038/nclimate3043, 2016.

Jöckel, P., Brenninkmeijer, C. A. M., and Lawrence, M. G.: Atmospheric response time of cosmogenic 14CO to changes in solar activity, Journal of Geophysical Research: Atmospheres, 105, 6737–6744, https://doi.org/10.1029/1999JD901140, 2000.

Kerkweg, A. and Jöckel, P.: The infrastructure MESSy submodels GRID (v1.0) and IMPORT (v1.0), Geoscientific Model Development Discussions, 8, 8607–8633, https://doi.org/10.5194/gmdd-8-8607-2015, 2015.

Kern, B.: Chemical interaction between ocean and atmosphere, Johannes Gutenberg-Universität, Mainz, Dissertation, 2013.

Kinne, S., O'Donnel, D., Stier, P., Kloster, S., Zhang, K., Schmidt, H., Rast, S., Giorgetta, M., Eck, T. F., and Stevens, B.: MAC-v1: A new global aerosol climatology for climate studies, Journal of Advances in Modeling Earth Systems, 5, 704–740, https://doi.org/10.1002/jame.20035, 2013.

Klocke, D., Quaas, J., and Stevens, B.: Assessment of different metrics for physical climate feedbacks, Climate Dynamics, 41, 1173–1185, https://doi.org/10.1007/s00382-013-1757-1, 2013.

Kunze, M., Godolt, M., Langematz, U., Grenfell, J., Hamann-Reinus, A., and Rauer, H.: Investigating the early Earth faint young Sun problem with a general circulation model, Planetary and Space Science, 98, 77–92, https://doi.org/10.1016/j.pss.2013.09.011, planetary evolution and life, 2014.

Li, J.: Gaussian Quadrature and Its Application to Infrared Radiation, Journal of the Atmospheric Sciences, 57, 753 – 765, https://doi.org/10.1175/1520-0469(2000)057<0753:GQAIAT>2.0.CO;2, 2000.

Li, J., Scinocca, J., Lazare, M., McFarlane, N., von Salzen, K., and Solheim, L.: Ocean Surface Albedo and Its Impact on Radiation Balance in Climate Models, Journal of Climate, 19, 6314 – 6333, https://doi.org/10.1175/JCLI3973.1, 2006.

Li, Z., Erb, A., Sun, Q., Liu, Y., Shuai, Y., Wang, Z., Boucher, P., and Schaaf, C.: Preliminary assessment of 20-m surface albedo retrievals from sentinel-2A surface reflectance and MODIS/VIIRS surface anisotropy measures, Remote Sensing of Environment, 217, 352–365, https://doi.org/10.1016/j.rse.2018.08.025, 2018.

Liu, J., Schaaf, C., Strahler, A., Jiao, Z., Shuai, Y., Zhang, Q., Roman, M., Augustine, J. A., and Dutton, E. G.: Validation of Moderate Resolution Imaging Spectroradiometer (MODIS) albedo retrieval algorithm: Dependence of albedo on solar zenith angle, Journal of Geophysical Research: Atmospheres, 114, https://doi.org/10.1029/2008JD009969, 2009.

Loeb, N. G., Wielicki, B. A., Doelling, D. R., Smith, G. L., Keyes, D. F., Kato, S., Manalo-Smith, N., and Wong, T.: Toward Optimal Closure of the Earth's Top-of-Atmosphere Radiation Budget, Journal of Climate, 22, 748 – 766, https://doi.org/10.1175/2008JCLI2637.1, 2009.

Loeb, N. G., Doelling, D. R., Wang, H., Su, W., Nguyen, C., Corbett, J. G., Liang, L., Mitrescu, C., Rose, F. G., and Kato, S.: Clouds and the Earth's Radiant Energy System (CERES) Energy Balanced and Filled (EBAF) Top-of-Atmosphere (TOA) Edition-4.0 Data Product, Journal of Climate, 31, 895 – 918, https://doi.org/10.1175/JCLI-D-17-0208.1, 2018.

Matthes, K., Funke, B., Andersson, M. E., Barnard, L., Beer, J., Charbonneau, P., Clilverd, M. A., Dudok de Wit, T., Haberreiter, M., Hendry, A., Jackman, C. H., Kretzschmar, M., Kruschke, T., Kunze, M., Langematz, U., Marsh, D. R., Maycock, A. C., Misios, S., Rodger, C. J., Scaife, A. A., Seppälä, A., Shangguan, M., Sinnhuber, M., Tourpali, K., Usoskin, I., van de Kamp, M., Verronen, P. T., and Versick, S.: Solar forcing for CMIP6 (v3.2), Geoscientific Model Development, 10, 2247–2302, https://doi.org/10.5194/gmd-10-2247-2017, 2017a.

Matthes, K., Funke, B., Kruschke, T., and Wahl, S.: input4MIPs.SOLARIS-HEPPA.solar.CMIP.SOLARIS-HEPPA-3-2, Earth System Grid Federation, VERSION YYYYMMDD, https://doi.org/10.22033/ESGF/input4MIPs.1122, 2017b.

Mauritsen, T. and Roeckner, E.: Tuning the MPI-ESM1.2 Global Climate Model to Improve the Match With Instrumental Record Warming by Lowering Its Climate Sensitivity, Journal of Advances in Modeling Earth Systems, 12, e2019MS002 037, https://doi.org/10.1029/2019MS002037, e2019MS002037 10.1029/2019MS002037, 2020.

Mauritsen, T., Stevens, B., Roeckner, E., Crueger, T., Esch, M., Giorgetta, M., Haak, H., Jungclaus, J., Klocke, D., Matei, D., Mikolajewicz, U., Notz, D., Pincus, R., Schmidt, H., and Tomassini, L.: Tuning the climate of a global model, Journal of Advances in Modeling Earth Systems, 4, https://doi.org/10.1029/2012MS000154, 2012.

Mauritsen, T., Bader, J., Becker, T., Behrens, J., Bittner, M., Brokopf, R., Brovkin, V., Claussen, M., Crueger, T., Esch, M., Fast, I., Fiedler, S., Fläschner, D., Gayler, V., Giorgetta, M., Goll, D. S., Haak, H., Hagemann, S., Hedemann, C., Hohenegger, C., Ilyina, T., Jahns, T., Jimenéz-de-la Cuesta, D., Jungclaus, J., Kleinen, T., Kloster, S., Kracher, D., Kinne, S., Kleberg, D., Lasslop, G., Kornblueh, L., Marotzke, J., Matei, D., Meraner, K., Mikolajewicz, U., Modali, K., Möbis, B., Müller, W. A., Nabel, J. E. M. S., Nam, C. C. W., Notz, D., Nyawira, S.-S., Paulsen, H., Peters, K., Pincus, R., Pohlmann, H., Pongratz, J., Popp, M., Raddatz, T. J., Rast, S., Redler, R., Reick, C. H., Rohrschneider, T., Schemann, V., Schmidt, H., Schnur, R., Schulzweida, U., Six, K. D., Stein, L., Stemmler, I., Stevens, B., von Storch, J.-S., Tian, F., Voigt, A., Vrese, P., Wieners, K.-H., Wilkenskjeld, S., Winkler, A., and Roeckner, E.: Developments in the MPI-M Earth System Model version 1.2 (MPI-ESM1.2) and Its Response to Increasing CO2, Journal of Advances in Modeling Earth Systems, 11, 998–1038, https://doi.org/10.1029/2018MS001400, 2019.

Meinshausen, M. and Vogel, E.: input4MIPs.UoM.GHGConcentrations.CMIP.UoM-CMIP-1-2-0, Earth System Grid Federation, VERSION YYYYMMDD, https://doi.org/10.22033/ESGF/input4MIPs.1118, 2016.

Meinshausen, M., Vogel, E., Nauels, A., Lorbacher, K., Meinshausen, N., Etheridge, D. M., Fraser, P. J., Montzka, S. A., Rayner, P. J., Trudinger, C. M., Krummel, P. B., Beyerle, U., Canadell, J. G., Daniel, J. S., Enting, I. G., Law, R. M., Lunder, C. R., O'Doherty, S., Prinn, R. G., Reimann, S., Rubino, M., Velders, G. J. M., Vollmer, M. K., Wang, R. H. J., and Weiss, R.: Historical greenhouse gas concentrations for climate modelling (CMIP6), Geoscientific Model Development, 10, 2057–2116, https://doi.org/10.5194/gmd-10-2057-2017, 2017.

Mlawer, E. J., Taubman, S. J., Brown, P. D., Iacono, M. J., and Clough, S. A.: Radiative transfer for inhomogeneous atmospheres: RRTM, a validated correlated-k model for the longwave, Journal of Geophysical Research: Atmospheres, 102, 16 663–16 682, https://doi.org/10.1029/97JD00237, 1997.

Morgenstern, O., Hegglin, M. I., Rozanov, E., O'Connor, F. M., Abraham, N. L., Akiyoshi, H., Archibald, A. T., Bekki, S., Butchart, N., Chipperfield, M. P., Deushi, M., Dhomse, S. S., Garcia, R. R., Hardiman, S. C., Horowitz, L. W., Jöckel, P., Josse, B., Kinnison, D., Lin, M., Mancini, E., Manyin, M. E., Marchand, M., Marécal, V., Michou, M., Oman, L. D., Pitari, G., Plummer, D. A., Revell, L. E., Saint-Martin, D., Schofield, R., Stenke, A., Stone, K., Sudo, K., Tanaka, T. Y., Tilmes, S., Yamashita, Y., Yoshida, K., and Zeng, G.: Review of the global models used within phase 1 of the Chemistry–Climate Model Initiative (CCMI), Geoscientific Model Development, 10, 639–671, https://doi.org/10.5194/gmd-10-639-2017, 2017.

Mote, P. W., Rosenlof, K. H., McIntyre, M. E., Carr, E. S., Gille, J. C., Holton, J. R., Kinnersley, J. S., Pumphrey, H. C., Russell, J. M., and Waters, J. W.: An atmospheric tape recorder: The imprint of tropical tropopause temperatures on stratospheric water vapor, Journal of Geophysical Research: Atmospheres, 101, 3989–4006, https://doi.org/10.1029/95JD03422, 1996.

Mote, P. W., Dunkerton, T. J., McIntyre, M. E., Ray, E. A., Haynes, P. H., and Russell III, J. M.: Vertical velocity, vertical diffusion, and dilution by midlatitude air in the tropical lower stratosphere, Journal of Geophysical Research: Atmospheres, 103, 8651–8666, https://doi.org/10.1029/98JD00203, 1998.

Myhre, G., Highwood, E. J., Shine, K. P., and Stordal, F.: New estimates of radiative forcing due to well mixed greenhouse gases, Geophysical Research Letters, 25, 2715–2718, https://doi.org/10.1029/98GL01908, 1998.

Müller, W. A., Jungclaus, J. H., Mauritsen, T., Baehr, J., Bittner, M., Budich, R., Bunzel, F., Esch, M., Ghosh, R., Haak, H., Ilyina, T., Kleine, T., Kornblueh, L., Li, H., Modali, K., Notz, D., Pohlmann, H., Roeckner, E., Stemmler, I., Tian, F., and Marotzke, J.: A Higher-resolution Version of the Max Planck Institute Earth System Model (MPI-ESM1.2-HR), Journal of Advances in Modeling Earth Systems, 10, 1383–1413, https://doi.org/10.1029/2017MS001217, 2018.

Naujokat, B.: An Update of the Observed Quasi-Biennial Oscillation of the Stratospheric Winds over the Tropics, Journal of Atmospheric Sciences, 43, 1873 – 1877, https://doi.org/10.1175/1520-0469(1986)043<1873:AUOTOQ>2.0.CO;2, 1986.

NCL: The NCAR Command Language (Version 6.6.2) [Software], UCAR/NCAR/CISL/TDD, Boulder, Colorado, https://doi.org/10.5065/D6WD3XH5, 2019.

Nissen, K. M., Matthes, K., Langematz, U., and Mayer, B.: Towards a better representation of the solar cycle in general circulation models, Atmospheric Chemistry and Physics, 7, 5391–5400, https://doi.org/10.5194/acp-7-5391-2007, 2007.

Oreopoulos, L. and Mlawer, E.: MODELING: The Continual Intercomparison of Radiation Codes (CIRC): Assessing Anew the Quality of GCM Radiation Algorithms, Bulletin of the American Meteorological Society, 91, 305 – 310, https://doi.org/10.1175/2009BAMS2732.1, 2010.

Oreopoulos, L., Mlawer, E., Delamere, J., Shippert, T., Cole, J., Fomin, B., Iacono, M., Jin, Z., Li, J., Manners, J., Räisänen, P., Rose, F., Zhang, Y., Wilson, M. J., and Rossow, W. B.: The Continual Intercomparison of Radiation Codes: Results from Phase I, Journal of Geophysical Research: Atmospheres, 117, https://doi.org/10.1029/2011JD016821, 2012.

Pincus, R. and Stevens, B.: Paths to accuracy for radiation parameterizations in atmospheric models, Journal of Advances in Modeling Earth Systems, 5, 225–233, https://doi.org/10.1002/jame.20027, 2013.

Pincus, R., Mlawer, E. J., Oreopoulos, L., Ackerman, A. S., Baek, S., Brath, M., Buehler, S. A., Cady-Pereira, K. E., Cole, J. N. S., Dufresne, J.-L., Kelley, M., Li, J., Manners, J., Paynter, D. J., Roehrig, R., Sekiguchi, M., and Schwarzkopf, D. M.: Radiative flux and forcing parameterization error in aerosol-free clear skies, Geophysical Research Letters, 42, 5485–5492, https://doi.org/10.1002/2015GL064291, 2015.

Pincus, R., Forster, P. M., and Stevens, B.: The Radiative Forcing Model Intercomparison Project (RFMIP): experimental protocol for CMIP6, Geoscientific Model Development, 9, 3447–3460, https://doi.org/10.5194/gmd-9-3447-2016, 2016.

Pincus, R., Buehler, S. A., Brath, M., Crevoisier, C., Jamil, O., Franklin Evans, K., Manners, J., Menzel, R. L., Mlawer, E. J., Paynter, D., Pernak, R. L., and Tellier, Y.: Benchmark Calculations of Radiative Forcing by Greenhouse Gases, Journal of Geophysical Research: Atmospheres, 125, e2020JD033 483, https://doi.org/10.1029/2020JD033483, e2020JD033483 10.1029/2020JD033483, 2020.

Pozzer, A., Jöckel, P., Kern, B., and Haak, H.: The Atmosphere-Ocean General Circulation Model EMAC-MPIOM, Geoscientific Model Development, 4, 771–784, https://doi.org/10.5194/gmd-4-771-2011, 2011.

Preisendorfer, R. W. and Mobley, C. D.: Albedos and Glitter Patterns of a Wind-Roughened Sea Surface, Journal of Physical Oceanography, 16, 1293 – 1316, https://doi.org/10.1175/1520-0485(1986)016<1293:AAGPOA>2.0.CO;2, 1986.

Ramaswamy, V., Collins, W., Haywood, J., Lean, J., Mahowald, N., Myhre, G., Naik, V., Shine, K. P., Soden, B., Stenchikov, G., and Storelvmo, T.: Radiative Forcing of Climate: The Historical Evolution of the Radiative Forcing Concept, the Forcing Agents and their Quantification, and Applications, Meteorological Monographs, 59, 14.1 – 14.101, https://doi.org/10.1175/AMSMONOGRAPHS-D-19-0001.1, 2018.

Rayner, N. A., Parker, D. E., Horton, E. B., Folland, C. K., Alexander, L. V., Rowell, D. P., Kent, E. C., and Kaplan, A.: Global analyses of sea surface temperature, sea ice, and night marine air temperature since the late nineteenth century, Journal of Geophysical Research: Atmospheres, 108, 4407, https://doi.org/10.1029/2002JD002670, 2003.

Richardson, T. B., Forster, P. M., Smith, C. J., Maycock, A. C., Wood, T., Andrews, T., Boucher, O., Faluvegi, G., Fläschner, D., Hodnebrog, , Kasoar, M., Kirkevåg, A., Lamarque, J.-F., Mülmenstädt, J., Myhre, G., Olivié, D., Portmann, R. W., Samset, B. H., Shawki, D., Shindell, D., Stier, P., Takemura, T., Voulgarakis, A., and Watson-Parris, D.: Efficacy of Climate Forcings in PDRMIP Models, Journal of Geophysical Research: Atmospheres, 124, 12 824–12 844, https://doi.org/10.1029/2019JD030581, 2019.

Rieger, V. S., Dietmüller, S., and Ponater, M.: Can feedback analysis be used to uncover the physical origin of climate sensitivity and efficacy differences?, Climate Dynamics, 49, 2831–2844, https://doi.org/10.1007/s00382-016-3476-x, 2017.

Righi, M., Andela, B., Eyring, V., Lauer, A., Predoi, V., Schlund, M., Vegas-Regidor, J., Bock, L., Brötz, B., de Mora, L., Diblen, F., Dreyer, L., Drost, N., Earnshaw, P., Hassler, B., Koldunov, N., Little, B., Loosveldt Tomas, S., and Zimmermann, K.: Earth System ModelEvaluation Tool (ESMValTool) v2.0 – technical overview, Geoscientific Model Development, 13, 1179–1199, https://doi.org/10.5194/gmd-13-1179-2020, 2020.

Roeckner, E., Arpe, K., Bengtsson, L., Christoph, M., Claussen, M., Dümenil, L., Esch, M., Giorgetta, M., Schlese, U., and Schulzweida, U.: The atmospheric general circulation model ECHAM-4, Model description and simulation of present-day climate, Report / Max-Planck-Institut für Meteorologie, 218, https://doi.org/10.17617/2.1781494, 1996.

Roeckner, E., Bäumel, G., Bonaventura, L., Brokopf, R., Esch, M., Giorgetta, M., Hagemann, S., Kirchner, I., Kornblueh, L., Manzini, E., Rhodin, A., Schlese, U., Schulzweida, U., and Tompkins, A.: The atmospheric general circulation model ECHAM5, PART I, Model description, Report / Max-Planck-Institut für Meteorologie, 349, https://doi.org/10.17617/2.995269, 2003.

Roeckner, E., Brokopf, R., Esch, M., Giorgetta, M., Hagemann, S., Kornblueh, L., Manzini, E., Schlese, U., and Schulzweida, U.: Sensitivity of Simulated Climate to Horizontal and Vertical Resolution in the ECHAM5 Atmosphere Model, Journal of Climate, 19, 3771–3791, https://doi.org/10.1175/JCLI3824.1, 2006.

Sander, R., Jöckel, P., Kirner, O., Kunert, A. T., Landgraf, J., and Pozzer, A.: The photolysis module JVAL-14, compatible with the MESSy standard, and the JVal PreProcessor (JVPP), Geoscientific Model Development, 7, 2653–2662, https://doi.org/10.5194/gmd-7-2653-2014, 2014.

Schaaf, C.: MODIS/Terra+Aqua BRDF/Albedo Gap-Filled Snow-Free Daily L3 Global 30ArcSec CMG V006, NASA EOSDIS Land Processes DAAC, accessed 2022-11-07, https://doi.org/10.5067/MODIS/MCD43GF.006, https://lpdaac.usgs.gov/products/mcd43gfv006/ downloaded from https://e4ftl01.cr.usgs.gov/MOTA/MCD43GF.006, 2019.

Schulzweida, U.: CDO User Guide (Version 2.1.0), Zenodo, https://doi.org/10.5281/zenodo.7112925, 2022.

Simmons, A., Soci, C., Nicolas, J., Bell, B., Berrisford, P., Dragani, R., Flemming, J., Haimberger, L., Healy, S., Hersbach, H., Horányi, A., Inness, A., Munoz-Sabater, J., Radu, R., and Schepers, D.: Global stratospheric temperature bias and other stratospheric aspects of ERA5 and ERA5.1, https://doi.org/10.21957/rcxqfmg0, 2020.

Smith, C. J., Kramer, R. J., Myhre, G., Forster, P. M., Soden, B. J., Andrews, T., Boucher, O., Faluvegi, G., Fläschner, D., Hodnebrog, , Kasoar, M., Kharin, V., Kirkevåg, A., Lamarque, J.-F., Mülmenstädt, J., Olivié, D., Richardson, T., Samset, B. H., Shindell, D., Stier, P., Takemura, T., Voulgarakis, A., and Watson-Parris, D.: Understanding Rapid Adjustments to Diverse Forcing Agents, Geophysical Research Letters, 45, 12,023–12,031, https://doi.org/10.1029/2018GL079826, 2018.

Stecher, L., Winterstein, F., Dameris, M., Jöckel, P., Ponater, M., and Kunze, M.: Slow feedbacks resulting from strongly enhanced atmospheric methane mixing ratios in a chemistry–climate model with mixed-layer ocean, Atmospheric Chemistry and Physics, 21, 731–754, https://doi.org/10.5194/acp-21-731-2021, 2021.

Stephens, G. L., Li, J., Wild, M., Clayson, C. A., Loeb, N., Kato, S., L'Ecuyer, T., Stackhouse, P. W., Lebsock, M., and Andrews, T.: An update on Earth's energy balance in light of the latest global observations, Nature Geoscience, 44, 691–696, https://doi.org/10.1038/ngeo1580, 2012.

Stevens, B., Giorgetta, M., Esch, M., Mauritsen, T., Crueger, T., Rast, S., Salzmann, M., Schmidt, H., Bader, J., Block, K., Brokopf, R., Fast, I., Kinne, S., Kornblueh, L., Lohmann, U., Pincus, R., Reichler, T., and Roeckner, E.: Atmospheric component of the MPI-M Earth System Model: ECHAM6, Journal of Advances in Modeling Earth Systems, 5, 146–172, https://doi.org/10.1002/jame.20015, 2013.

Stuber, N., Sausen, R., and Ponater, M.: Stratosphere adjusted radiative forcing calculations in a comprehensive climate model, Theoretical and Applied Climatology, 68, 125–135, https://doi.org/10.1007/s007040170041, 2001.

Sun, Q., Wang, Z., Li, Z., Erb, A., and Schaaf, C. B.: Evaluation of the global MODIS 30 arc-second spatially and temporally complete snow-free land surface albedo and reflectance anisotropy dataset, International Journal of Applied Earth Observation and Geoinformation, 58, 36–49, https://doi.org/10.1016/j.jag.2017.01.011, 2017.

Tanre, D., Geleyn, J., and Slingo, J.: First results of an advanced aerosol-radiation interaction in ECMWF low resolution global model, in: Aerosols and Their Climatic Effects, edited by Gerber, H. and Deepak, A., 133–177, 1984.

The MESSy Consortium: The Modular Earth Submodel System (2.55.2), Zenodo, https://doi.org/10.5281/zenodo.8360276, 2021.

The MESSy Consortium: The Modular Earth Submodel System (2.55.2_92d5b399_radiation), Zenodo, https://doi.org/10.5281/zenodo.8382302, 2023.

Thomas, M. A.: Simulation of the climate impact of Mt. Pinatubo eruption using ECHAM5, Ph.D. thesis, University of Hamburg, https://doi.org/10.17617/2.994206, 2008.

Trenberth, K. E., Fasullo, J. T., and Kiehl, J.: Earth's Global Energy Budget, Bulletin of the American Meteorological Society, 90, 311 – 324, https://doi.org/10.1175/2008BAMS2634.1, 2009.

Wild, M.: The global energy balance as represented in CMIP6 climate models, Climate Dynamics, 55, 553–577, https://doi.org/10.1007/s00382-020-05282-7, 2017.

Wild, M., Folini, D., Hakuba, M. Z., Schär, C., Seneviratne, S. I., Kato, S., Rutan, D., Ammann, C., Wood, E. F., and König-Langlo, G.: The energy balance over land and oceans: an assessment based on direct observations and CMIP5 climate models, Climate Dynamics, 44, 3393–3429, https://doi.org/10.1007/s00382-014-2430-z, 2015.

Winterstein, F. and Jöckel, P.: Methane chemistry in a nutshell – the new submodels CH4 (v1.0) and TRSYNC (v1.0) in MESSy (v2.54.0), Geoscientific Model Development, 14, 661–674, https://doi.org/10.5194/gmd-14-661-2021, 2021.

Winterstein, F., Tanalski, F., Jöckel, P., Dameris, M., and Ponater, M.: Implication of strongly increased atmospheric methane concentrations for chemistry–climate connections, Atmospheric Chemistry and Physics, 19, 7151–7163, https://doi.org/10.5194/acp-19-7151-2019, 2019.

Yang, F., Kumar, A., Wang, W., Juang, H.-M. H., and Kanamitsu, M.: Snow–Albedo Feedback and Seasonal Climate Variability over North America, Journal of Climate, 14, 4245 – 4248, https://doi.org/10.1175/1520-0442(2001)014<4245:SAFASC>2.0.CO;2, 2001.

Zelinka, M. D., Myers, T. A., McCoy, D. T., Po-Chedley, S., Caldwell, P. M., Ceppi, P., Klein, S. A., and Taylor, K. E.: Causes of Higher Climate Sensitivity in CMIP6 Models, Geophysical Research Letters, 47, e2019GL085 782, https://doi.org/10.1029/2019GL085782, e2019GL085782 10.1029/2019GL085782, 2020.

Zängl, G., Reinert, D., Rípodas, P., and Baldauf, M.: The ICON (ICOsahedral Non-hydrostatic) modelling framework of DWD and MPI-M: Description of the non-hydrostatic dynamical core, Quarterly Journal of the Royal Meteorological Society, 141, 563–579, https://doi.org/10.1002/qj.2378, 2015.